AGU PUBLICATIONS

JGR

Journal of Geophysical Research: Atmospheres

RESEARCH ARTICLE
10.1002/2015JD024650

Key Points:
- E-Tagging approach to calculate atmospheric water residence times
- Atmospheric residence time of transpired water until falling out as precipitation is longer than that of directly evaporated water
- Model allows studying timescales of the atmospheric branch of the hydrological cycle under global warming

Correspondence to:
J. Wei,
jianhui.wei@kit.edu

Citation:
Wei, J., H. R. Knoche, and H. Kunstmann (2016), Atmospheric residence times from transpiration and evaporation to precipitation: An age-weighted regional evaporation tagging approach, *J. Geophys. Res. Atmos.*, *121*, 6841–6862, doi:10.1002/2015JD024650.

Received 15 DEC 2015
Accepted 24 MAY 2016
Accepted article online 30 MAY 2016
Published online 23 JUN 2016

Atmospheric residence times from transpiration and evaporation to precipitation: An age-weighted regional evaporation tagging approach

Jianhui Wei[1,2], Hans Richard Knoche[1], and Harald Kunstmann[1,2]

[1] Institute of Meteorology and Climate Research (IMK-IFU), Karlsruhe Institute of Technology, Campus Alpin, Garmisch-Partenkirchen, Germany, [2] Institute of Geography, University of Augsburg, Augsburg, Germany

Abstract The atmospheric water residence time is a fundamental descriptor that provides information on the timescales of evaporation and precipitation. In this study, a regional climate model-based evaporation tagging algorithm is extended with an age tracer approach to calculate moisture residence times, defined as time between the original evaporation and the returning of water masses to the land surface as precipitation. Our case study addresses how long this time is for the transpired and for the direct evaporated moisture. Our study region is the Poyang Lake region in Southeast China, the largest freshwater lake in the country. We perform simulations covering the period from October 2004 to December 2005. In 2005, 11% of direct evaporated water (10% of transpired water) precipitates locally. Direct evaporated water accounts for 64% and transpired water for 36% of the total tagged moisture with a mean age of around 36 h for both. Considering precipitation, a large proportion (69%) originates from direct evaporated water with a mean atmospheric residence time of 6.6 h and a smaller amount from transpired water with a longer residence time of 10.7 h. Modulated by the East Asian monsoon, the variation of the meteorological conditions, the magnitude of the partitioned moisture, and the corresponding residence time patterns change seasonally and spatially and reveal the different fate of transpired and direct evaporated water in the atmospheric hydrological cycle. We conclude that our methodological approach has the potential to be used for addressing how timescales of the hydrological cycle changes regionally under global warming.

1. Introduction

It is understood that human-induced global warming leads to an enhancement of the evaporation process and thereby to an acceleration of the atmospheric branch of the hydrological cycle [*IPCC*, 2014]. This is supported by empirical evidence [*Huntington*, 2006], modeling studies [*Allen and Ingram*, 2002], and theoretical expectation based on the Clausius-Clapyeron relation [*Held and Soden*, 2006]. Although the acceleration of the hydrological cycle is generally acknowledged, the details of how regional hydrological cycles will change under global warming is still a challenging question [*Trenberth*, 1999].

The response of the hydrological cycle to the climate regime can be studied by investigating, for example, the relationship between evaporation (E) and precipitation (P), particularly the atmospheric water residence time, here defined as time between the original evaporation and the returning of its respective water masses to the land surface as precipitation. This concept is used in various studies [*Trenberth*, 1998; *Numaguti*, 1999; *James*, 2003; *van der Ent and Savenije*, 2011; *Tuinenburg et al.*, 2012; *Wang-Erlandsson et al.*, 2014; *van der Ent et al.*, 2014; *Läderach and Sodemann*, 2016]. It provides additional information on the timescales of evaporation and precipitation and reflects the complexity of the atmospheric water pathways and the phase changes including the formation of precipitation. In addition, a probability density function of residence times, hereafter referred to as residence time distribution (RTD), allows characterization of the natural atmospheric hydrological cycle for different regimes and seasons. Apart from atmospheric science, this concept has been also extensively applied in numerous fields of geophysics [*McGuire and McDonnell*, 2006; *Harman and Kim*, 2014], e.g., in the hydrologic studies on rainfall-runoff responses [*Hrachowitz et al.*, 2013] and on groundwater age distributions [*Gomez and Wilson*, 2013]. A detailed overview and interpretation of this concept are given by *Bolin and Henning* [1973], *Zuber* [1986], and *McGuire and McDonnell* [2006].

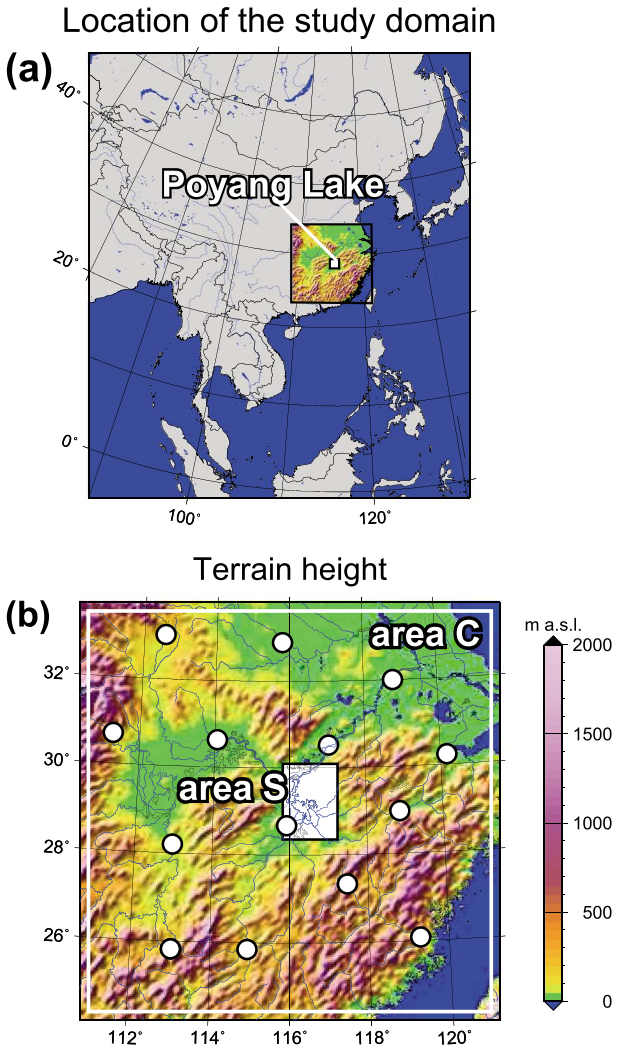

Figure 1. (a) Location of the model domain with the Poyang Lake and (b) terrain height (meters above sea level) of the model domain. Rivers, lakes, and the ocean are shown in blue. The tagging source area (area S: the Poyang Lake region) lies within the white-shaded rectangle. The large white rectangle (area C: the model domain except a small boundary zone), nearly representing Southeast China, marks the regions where the atmospheric water residence times are analyzed. The individual circles represent IGRA radiosonde stations used for wind validation of the MM5 simulation.

There are only a few studies calculating atmospheric water residence times. By using an atmospheric general circulation model in conjunction with moisture tracers, *Numaguti* [1999] investigated the mean age of the precipitated water from the oceanic and from the continental origins in Eurasia. A Lagrangian particle dispersion model in which particles act as tracers has been employed for assessing the exchange rate of air parcels between stratosphere and troposphere on a global scale *James* [2003]. *Trenberth* [1998] used a function for depletion of precipitable water by precipitation to estimate the global mean residence time of atmospheric moisture. Additionally, environmental tracers and passive modeled tracers are utilized often as a combined observational and modeling approach to calculate residence times and corresponding distributions *Gomez and Wilson* [2013].

Recently, the RTD for water evaporated from the Ganges basin has been estimated by *Tuinenburg et al.* [2012] using a quasi-isentropic moisture tracking scheme. The global atmospheric lifetime of recycled moisture was studied by *van der Ent et al.* [2014] using an Eulerian offline model. *Läderach and Sodemann* [2016] provided a revised global picture of the residence time of atmospheric moisture by using Lagrangian moisture source diagnostics. These and similar other modeling studies either have been conducted on large scales with a coarse resolution or have used relatively simple schemes for atmospheric dynamical and physical processes. This may limit the accuracy of estimates of atmospheric residence times, e.g., due to an inadequate representation of the complex atmospheric features, especially, when directional wind shear is present or strong moist convection happens [*Goessling and Reick*, 2013; *van der Ent et al.*, 2013].

To overcome these difficulties, sophisticated three-dimensional regional climate models (RCMs) with a built-in evaporation tagging (E-Tagging) algorithm are suitable for local-scale moisture tracking studies over a monsoon-controlled region *van der Ent et al.* [2013]. An E-Tagging algorithm was firstly implemented in a RCM by *Sodemann et al.* [2009]. *Knoche and Kunstmann* [2013] and *Arnault et al.* [2016] built an E-Tagging algorithm into the Fifth-Generation Mesoscale Model (MM5) [*Dudhia*, 1993; *Grell et al.*, 1994] and the Weather Research and Forecasting Model, respectively.

Previously, *Scott et al.* [1997] and *Lohmann and Wood* [2003] quantified the response timescales for the components of the simulated evaporation within the land surface models through convolution of precipitation, both globally and regionally. Recently, *van der Ent et al.* [2014] first investigated the timescales of direct evaporation and transpiration in the context of moisture recycling. *Wei et al.* [2015] extended the model to track

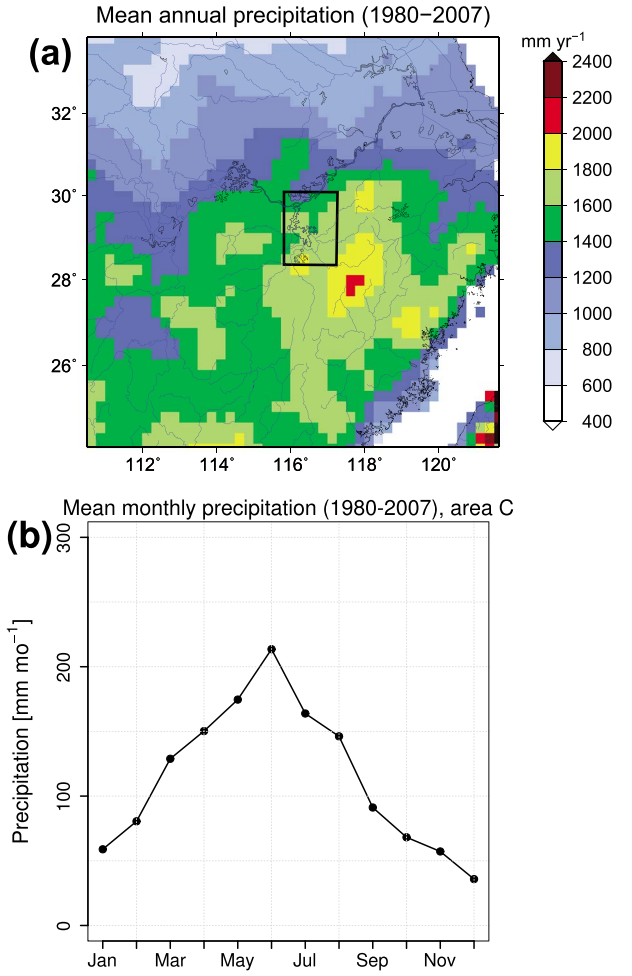

Figure 2. Mean precipitation in the years 1980–2007 (Data source: APHRODITE at 0.25° × 0.25° resolution): (a) spatial distribution of the mean annual precipitation (mm yr^{-1}) and (b) annual variation of the mean monthly precipitation (mm mo^{-1}) averaged over area C.

transpiration and direct evaporation separately. The extended model allows tagging of the moisture transpired or directly evaporated from a given source area. The model then follows the pathways of the tagged moisture across the atmosphere until it returns to the land surface as precipitation or leaves the model domain. In this study, the E-Tagging partitioning algorithm is extended again by including a mechanism to calculate the atmospheric water residence times for moisture originating from a specific region.

We apply the newly extended model in the research scope of land-atmosphere interactions to a case study for the Poyang Lake region. The Poyang Lake (29°05′N, 116°17′E) is located in the center of Southeast China (see Figure 1). This lake is the largest freshwater lake in China covering on average a surface area of 3500 km^2 and containing a water volume of approximately 25.2 km^3. It is mainly fed by the inflow from five tributaries in the Poyang Lake basin. The lake and its surrounding wetlands (the Poyang Lake region), dominated by irrigated paddy rice, perform crucial hydrologic and ecologic functions for flood control [*Shankman et al.*, 2012; *Zhang et al.*, 2012] and for maintenance of biodiversity *Jiao* [2009]. In this region, precipitation strongly influences the spatial and temporal distribution of water availability, which eventually affects water-dependent agriculture and hydroecologic functions. Many studies reported that the frequency of heavy precipitation [*Ye*, 2014], severe floods [*Shankman et al.*, 2006] and droughts [*Feng et al.* 2012] has significantly increased in the past 30 years and is predicted to continue increasing in the near future due to human-induced regional climate change. Therefore, it is of crucial significance to further understand the atmospheric part of land-atmosphere interactions for this region. We assume that the Poyang Lake region in Southeast China is a suited case study test site because of the land surface characteristics (e.g., water bodies, soil, and vegetation) and the complex atmospheric dynamics (i.e., the East Asian monsoon system).

The climate of Southeast China is determined by the East Asian monsoon system [*Trenberth et al.*, 2000; *Zhu and Chen*, 2002]. In winter, the monsoon is closely connected to the Siberian high in the north and cool and dry moisture are transported by the prevailing northeasterly winds [*Wu et al.*, 2006]. In summer, the main low-level streams transport moisture toward China [*Chow et al.*, 2008], and the origin is temporally varying between the Indian Ocean and the Bay of Bengal, the South China Sea, and the western North Pacific Ocean. The precipitation variability over Southeast China is large, both on spatial and temporal scales (Figure 2). The range of total mean annual precipitation is from less than 600 mm yr^{-1} in the north to more than 2000 mm yr^{-1} in an area closely southeast to the Poyang Lake basin (Figure 2a). The monthly variability of precipitation (Figure 2b) is dominated by the variations of the strength of the summer monsoon [*Ding and Chan*, 2005], with the rainy period from April to June. In addition, rainfall from January to March over southeastern China is closely related to the interannual variations of the winter monsoon [*Zhou*, 2011].

The objectives of this study are (1) to introduce and demonstrate a process-based, three-dimensional regional climate model-based algorithm for the calculation of atmospheric water residence times, (2) to apply this extended model for the first time in Southeast China, and (3) to investigate spatial and temporal variations of atmospheric residence times of the direct evaporated and transpired water from the Poyang Lake region. Thus, the specific questions we address in this study are (1) to what extent do atmospheric residence times of transpired moisture differ from these of directly evaporated moisture? (2) What are the mechanisms behind these differences? Following this idea, we apply the age-weighted extended model to estimate how long the time is between the original evaporation (transpiration and direct evaporation) in the Poyang Lake region and the subsequent precipitation. To our knowledge, an RCM-based algorithm for calculating atmospheric water residence times has not yet been used for the subtropical and mountainous Southeast China.

2. Model and Methodology

In our study, the Fifth-Generation Pennsylvania State University/National Center for Atmospheric Research Mesoscale Model (MM5) version 3.5 [*Dudhia*, 1993; *Grell et al.*, 1994] is used as the basic model for the implementation of the age-weighted E-Tagging partitioning algorithm. MM5 is a regional, process-based nonhydrostatic model which simulates the behavior of a coupled dynamical system: atmosphere and soil and snow cover and vegetation. As a limited area model, it allows representation of the small-scale meteorological fields driven by external simulations (e.g., general circulation model simulations) or reanalysis data (e.g., ERA-Interim).

2.1. E-Tagging Partitioning Algorithm

The concept of the E-Tagging algorithm is to add a second numerical formulation of the atmospheric hydrological cycle for the tagged moisture: evaporated water from a selected region is "tagged" when entering the atmosphere. Then, the tagged moisture undergoes the same atmospheric processes as the total moisture, including returning to the land surface as precipitation or leaving the model domain. This E-Tagging algorithm has been implemented by *Knoche and Kunstmann* [2013] in MM5 to investigate the fate of the tagged moisture and has been further extended by *Wei et al.* [2015] to separately quantify the contribution of the individual evaporation components, i.e., direct evaporation and transpiration, to regional precipitation.

2.2. Age Weighting Extension

For the calculation of the atmospheric water residence times, additional model extensions concerning the "age weighting" are introduced. Analogously to the implementation of the E-Tagging algorithm into an RCM by adding a second atmospheric hydrological cycle for the tagged moisture, additional information on the timescales can be gained by adding a *third* level of atmospheric "hydrological" cycle information in the RCM code that accounts for the age-weighted tagged moisture. New model variables representing the age-weighted tagged water components are defined, and an additional equation set controlling the evolution of the age-weighted tagged water components is formulated.

The original MM5 moisture equations describing grid-scale transport, subgrid-scale transport due to turbulence and diffusion, phase transitions, and the downward movement of precipitating water components are duplicated again in the code. Besides the original equation set for the total moisture components q_k (kg kg^{-1}) (i.e., water vapor q_v, cloud water q_c, cloud ice q_i, rain water q_r, and snow q_s) and the second equation set for the tagged moisture components $q_{k,\mathrm{tag}}$ (kg kg^{-1}) in the extended MM5 model [see *Knoche and Kunstmann*, 2013, equations (4) and (5)], the new third equation set accounts for the age-weighted tagged moisture components $\tilde{q}_{k,\mathrm{tag}}$ (kg kg^{-1} s) and is as follows:

$$\begin{aligned}\frac{\partial}{\partial t}(p^*\tilde{q}_{k,\mathrm{tag}}) = &-\left\{ m^2\left[\frac{\partial(p^*\tilde{q}_{k,\mathrm{tag}}m^{-1}u)}{\partial x}+\frac{\partial(p^*\tilde{q}_{k,\mathrm{tag}}m^{-1}v)}{\partial y}\right]+\frac{\partial(p^*\tilde{q}_{k,\mathrm{tag}}\dot{\sigma})}{\partial\sigma}\right\}\\ &+\tilde{q}_{k,\mathrm{tag}}\left\{ m^2\left[\frac{\partial(p^*m^{-1}u)}{\partial x}+\frac{\partial(p^*m^{-1}v)}{\partial y}\right]+\frac{\partial(p^*\dot{\sigma})}{\partial\sigma}\right\}\\ &+\Phi_{\mathrm{sub}}(\tilde{q}_{k,\mathrm{tag}})+p^*C_{\tilde{q}_{k,\mathrm{tag}}}+\Phi_{\mathrm{prc}}(\tilde{q}_{k,\mathrm{tag}})+S_{\tilde{q}_{k,\mathrm{tag}}}.\end{aligned} \tag{1}$$

Here $p^* = p_{s0} - p_t$ (Pa) is the time invariant difference between the reference pressure p_{s0} at the surface and the constant pressure p_t at the model top. x (m) and y (m) are the two horizontal coordinates and u (m s^{-1}) and v (m s^{-1}) the two horizontal wind velocities. The dimensionless variable σ is the generalized vertical coordinate with $\dot{\sigma}$ (s^{-1}) as its time derivative. m is the map projection factor.

Φ_{sub} (Pa kg kg^{-1} s^{-1} s), $p^* C_{\tilde{q}_{k,\text{tag}}}$ (Pa kg kg^{-1} s^{-1} s), and Φ_{prc} (Pa kg kg^{-1} s^{-1} s) represent the subgrid-scale transport, the phase transitions, and the (relative) downward movement of precipitating water components, respectively. $S_{\tilde{q}_{k,\text{tag}}}$ (Pa kg kg^{-1} s^{-1} s) denotes the source term due to advancing time for the age-weighted tagged moisture components. The transition rates $C_{\tilde{q}_{k,\text{tag}}}$ (kg kg^{-1} s^{-1} s) are proportional to the original transition rates C_{q_k} (kg kg^{-1} s^{-1}) and the ratio of age-weighted tagged moisture components $\tilde{q}_{k,\text{tag}}$ to original total moisture components q_k

$$C_{\tilde{q}_{k,\text{tag}}} = C_{q_k} \cdot \tilde{q}_{k,\text{tag}} / q_k. \tag{2}$$

For the solution of the differential equation (1) a time splitting scheme is applied to increase efficiency of computation. First, the equation without the term $S_{\tilde{q}_{k,\text{tag}}}$ is integrated to obtain preliminary age-weighted tagged moisture components $\tilde{q}^{n*}_{k,\text{tag}}$ from previous time step n due to atmospheric transport and phase change processes. The spatial and temporal finite differencing schemes for equation (1) in this study are the same as for equations (4) and (5) in *Knoche and Kunstmann* [2013]. Then, regarding the time advancing for $\tilde{q}_{k,\text{tag}}$, the remaining term $S_{\tilde{q}_{k,\text{tag}}}$ of equation (1) is integrated. Since the age of the tagged moisture increases linearly with time, the numerical solution is given as

$$\tilde{q}^{n+1}_{k,\text{tag}} = \tilde{q}^{n*}_{k,\text{tag}} + q^{n+1}_{k,\text{tag}} \cdot \Delta T, \tag{3}$$

where the time constant term p^* appearing in equation (1) is omitted. ΔT (s) denotes the model time step length. Initially, the tagged and the age-weighted tagged moisture components are set to zero.

The formation of tagged moisture begins with the evaporation process at the land surface. Simultaneously, the formation of the atmospheric age-weighted moisture is triggered and then tracked through all atmospheric processes until precipitating. The extended model then allows to calculate the atmospheric residence times of moisture by

$$\tau_k = \tilde{q}_{k,\text{tag}} / q_{k,\text{tag}} \tag{4}$$

and the atmospheric residence times of precipitated water by

$$T_P = \tilde{P}_{\text{tag}} / P_{\text{tag}}. \tag{5}$$

P_{tag} (mm s^{-1}) denotes the tagged precipitation originating from a predefined source area, while $\tilde{P}_{\text{tag}}$ (mm s^{-1} s) denotes the age-weighted tagged precipitation.

In the context of E-Tagging partitioning, the atmospheric residence times τ_{k,E_d} of tagged moisture components $q_{k,\text{tag}E_d}$ formed by direct evaporation E_d and the atmospheric residence times τ_{k,E_t} of tagged moisture components $q_{k,\text{tag}E_t}$ formed by transpiration E_t are defined as

$$\tau_{k,E_d} = \tilde{q}_{k,\text{tag}E_d} / q_{k,\text{tag}E_d} \tag{6}$$

$$\tau_{k,E_t} = \tilde{q}_{k,\text{tag}E_t} / q_{k,\text{tag}E_t}. \tag{7}$$

Similarly, the atmospheric residence times T_{P,E_d} of tagged precipitation P_{tag,E_d} contributed by direct evaporation and the atmospheric residence times T_{P,E_t} of tagged precipitation P_{tag,E_t} contributed by transpiration are defined as

$$T_{P,E_d} = \tilde{P}_{\text{tag},E_d} / P_{\text{tag},E_d} \tag{8}$$

$$T_{P,E_t} = \tilde{P}_{\text{tag},E_t} / P_{\text{tag},E_t}. \tag{9}$$

3. The Experimental Design

For the general configuration of MM5 we closely follow the selection as chosen in *Knoche and Kunstmann* [2013] and *Wei et al.* [2015]. It consists of the Medium Range Forecast Model [*Hong and Pan*, 1996] for planetary boundary layer modeling and turbulence parametrization, the Dudhia scheme [*Dudhia*, 1989] and the Rapid Radiation Transfer Model [*Mlawer et al.*, 1997] for shortwave and longwave radiation calculations, the explicit microphysics Mixed-Phase Reisner 1 scheme [*Reisner et al.*, 1998], and the multilayer land surface model, Oregon State University Land Surface Model [*Chen and Dudhia*, 2001]. More details about the model are given in *Dudhia* [1993] and *Grell et al.* [1994].

The experimental simulations cover 15 months from October 2004 to December 2005. Initial and lateral boundary conditions are taken from the European Centre for Medium Range Weather Forecasts Interim reanalysis. To find an optimal MM5 model setup, we have performed several preliminary simulation experiments with altered domain size and grid spacing. For evaluation, we used the 0.25° gridded daily data set APHRODITE_V1003R1 (Asian Precipitation Highly Resolved Observational Data Integration Towards Evaluation of Water Resources [*Yatagai et al.*, 2009, 2012] and the 0.5° gridded monthly data set FLUXNET MTE (Multi-Tree Ensemble) [*Jung et al.*, 2009, 2010, 2011] as reference data set for precipitation and (total) evaporation. According to the model performance analysis (details shown in *Wei et al.* [2015]), we favor a model domain covering Southeast China (see Figure 1) with a horizontal resolution of 4.5 km and 240 × 240 grid cells. The vertical grid consists of 33 vertical levels up to 50 hPa, with refined layers in the lower part of the atmosphere. Model equations are integrated with a basic time step of 10 s.

For purpose of further evaluation of the MM5 model performance, IGRA (the Integrated Global Radiosonde Archive) [*Durre et al.*, 2006, 2008] is used as reference data for the simulated wind fields. The IGRA database provides long-term daily radiosonde observations (e.g., wind speed and wind direction data) from more than 1500 stations globally. It is the largest and most comprehensive collection of quality-assured soundings and readily available.

In this study, we focus on the atmospheric residence times of water from a moisture source area including the Poyang Lake and its surrounding wetlands (around 2.5×10^4 km^2), hereafter referred to as area S (see Figure 1). According to the global 25-category data from U.S. Geological Survey (USGS), the area of the Poyang Lake covers 13.5% of the source area S. Around the lake, irrigated paddy rice is the dominant vegetation type, accounting for about 47.6%. The model domain except a small boundary zone (area C) is used as region of interest (i.e., named target area) where the tagged moisture and the tagged precipitation are examined in the analysis. We performed three long-term model runs for the period from October 2004 to December 2005 to track the total evaporated, direct evaporated, and transpired water. To assess the atmospheric residence times of the total evaporated, direct evaporated, and transpired water and the corresponding intra-annual/seasonal variability, we perform our analysis for the period of the entire year 2005 after 3 months spin-up time on a monthly scale. To demonstrate the age-weighted regional E-Tagging approach, we consider the formation of tagged and age-weighted tagged moisture in the first 48 h during the spin-up period of the simulation for the (total) evaporated water.

4. Results and Discussion

4.1. Validation of Simulated Wind and Precipitation

Simulated wind components from MM5 can be compared with observational data set from IGRA. Figure 3 shows the vertical profiles of wind components from MM5 and IGRA, averaged for 14 radiosonde stations by month for the year 2005. The variations of simulated wind speed and direction with height and season show comparatively good agreement with the data derived from the station observation. For the zonal wind component, a difference between simulated and observed winds is small from January to May, tends to be larger (underestimation of around 0.26 m s^{-1}) during the warm season (June–September), and becomes small again from October to December (Figure 3a). Due to the onset and retreat of the East Asian summer monsoon, changes in the direction of the meridional wind component are observed in the lower part of the atmosphere (below 800 hPa) from IGRA (Figure 3b). These changes are also well captured by the model, with an overestimation of around 0.5 m s^{-1} in summer.

Annual total precipitation for area C for the whole year 2005 shows a fairly good agreement (correlation coefficient: 0.64; $p < 0.001$) between MM5 and APHRODITE (Figure 4a). Averaged over all grid points in area C, the relative difference between simulated and observed annual total precipitation is −12%. On the monthly scale

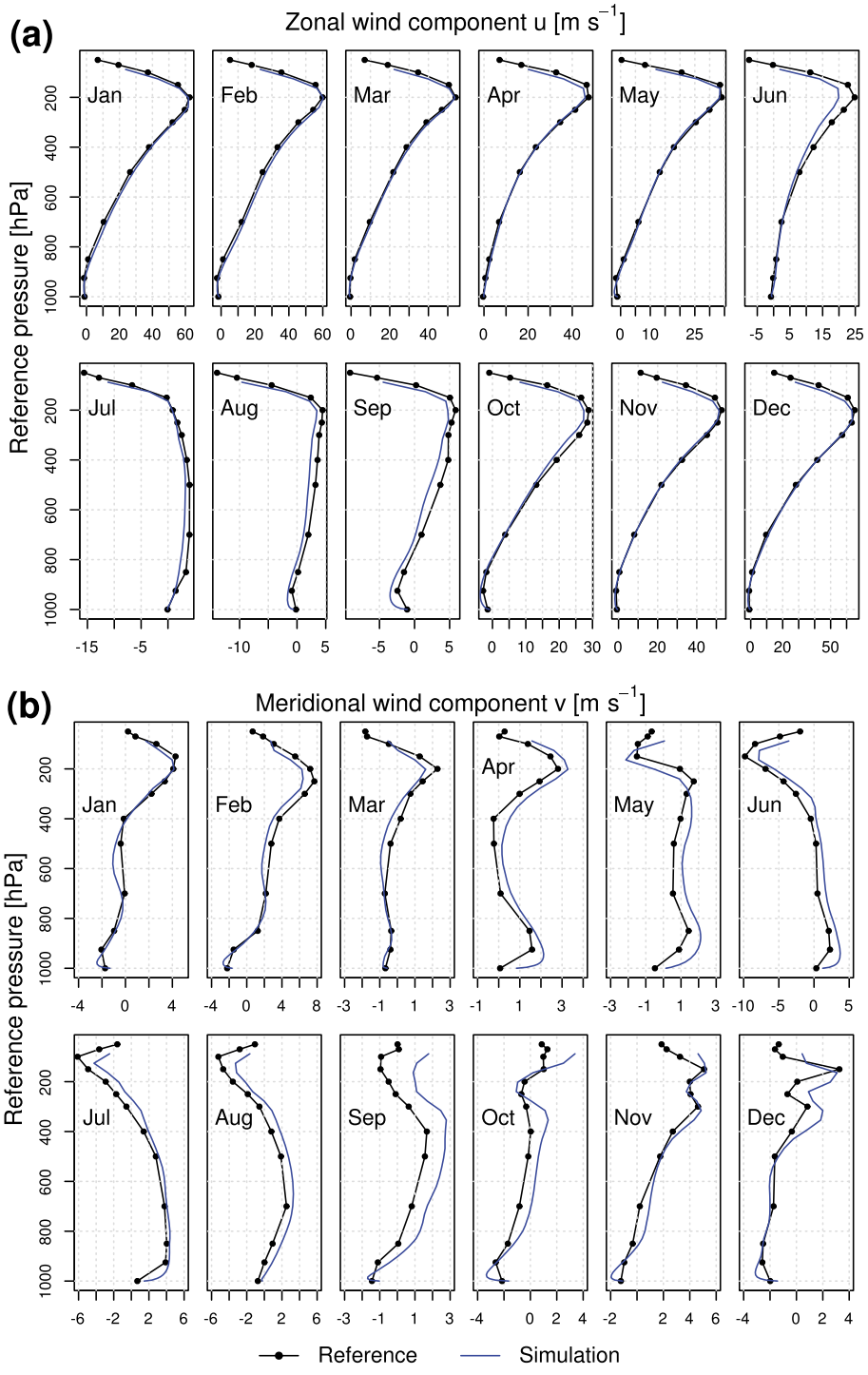

Figure 3. Comparison of simulation (blue line) and reference (black line) data for vertical profile of wind components: (a) zonal velocity u (m s^{-1}) and (b) meridional velocity v (m s^{-1}). The observational wind components from IGRA reference data are averaged for 14 radiosonde stations (shown in Figure 1b) for each month in 2005. Our simulated wind components are accordingly averaged over nine grid points surrounding each station for each model layer and for the same period under investigation.

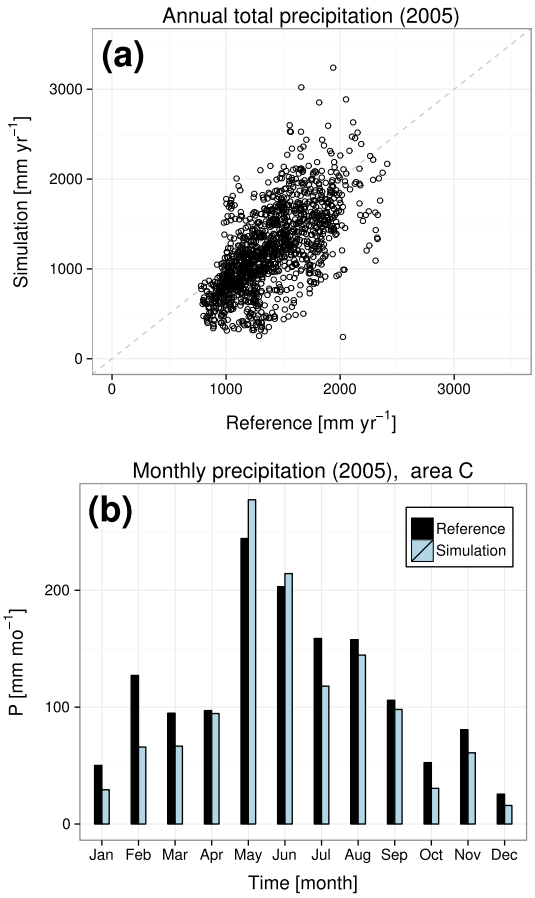

Figure 4. (a) Comparison between APHRODITE-derived and MM5-derived annual total precipitation (mm yr^{-1}) for area C for 2005. (b) Area-aggregated, monthly time series of precipitation (mm mo^{-1}) for area C, derived from APHRODITE (black bars) and from MM5 (blue bars).

(Figure 4b), the MM5 model can reasonably represent the annual cycle of precipitation. The simulated precipitation is below the observed values, with the exception of May and June. Overall, the simulated winds and precipitation are reasonably reproduced, and it is concluded that our model setup allows to address estimates of atmospheric water residence times for this study region.

4.2. Illustration of the Dynamical Evolution

To demonstrate our age-weighted E-Tagging algorithm we consider the first 48 h of the model run as simulating the formation of tagged and age-weighted tagged moisture originating from the (total) evaporated water. The results are shown in Figures 5 and 6. The evolutions of the tagged moisture, of the age-weighted tagged moisture, and of the corresponding atmospheric residence times are displayed for five selected times between 00:00 UTC 1 and 24:00 UTC 2 in October 2004. The figures reveal the variations due to differences of the evaporation and of the atmospheric transport conditions.

Figure 5 shows the spatial distribution of the column-integrated total tagged moisture $Q_{t,\mathrm{tag}}$ (consisting of water vapor, cloud water, cloud ice, rain water, and snow) (Figures 5a, 5d, 5g, 5j, and 5m), the age-weighted total tagged moisture $\tilde{Q}_{t,\mathrm{tag}}$ (Figures 5b, 5e, 5h, 5k, and 5n), and the age τ_{Q_t} of the total tagged moisture (Figures 5c, 5f, 5i, 5l, and 5o) over Southeast China at the selected five times. In addition, the hourly mean of the simulated horizontal wind field at 10 m is shown as well. At the start of the simulation at 08:00 in the Chinese Standard Time (CST) zone (00:00 UTC) on 1 October 2004, tagged moisture and age-weighted tagged moisture are set to zero. After that evaporated water from the source area S is tagged when entering the atmosphere, and the age weighting processes of tagged moisture components are triggered. Then, both the tagged moisture $Q_{t,\mathrm{tag}}$ and the age-weighted tagged moisture $\tilde{Q}_{t,\mathrm{tag}}$ undergo the same atmospheric processes (i.e., transport by the wind fields and phase transitions) as the (original) total moisture. Figures 5a and 5b demonstrate the transport and spreading controlled by the wind fields after 1 h of simulation. Finally, the tagged moisture and the age-weighted tagged moisture can leave the model domain (see Figures 5d, 5g, 5e, and 5h) or can return to the land surface as tagged precipitation and age-weighted tagged precipitation. Moreover, during these 48 h, the role of precipitation is not yet significant. The day-night change in temperature leads to the fluctuation of the amount of evaporated water and thereby impacts the variations of the $Q_{t,\mathrm{tag}}$ and the $\tilde{Q}_{t,\mathrm{tag}}$ patterns. Figures 5g and 5h show that little tagged moisture and little age-weighted tagged moisture are found over the source area S due to the limited water evaporated in the cold hours after midnight (i.e., 02:00 CST 2 October). With incoming radiation and rising temperature in the second day (i.e., 2 October), $Q_{t,\mathrm{tag}}$ and $\tilde{Q}_{t,\mathrm{tag}}$ increase and undergo the transport and spreading processes again (see Figures 5j, 5m, 5k, and 5n).

The mean age τ_{Q_t} patterns of the total tagged moisture in Figures 5c, 5f, 5i, 5l, and 5o are generally controlled by two factors: the magnitudes of the newly tagged evaporated water compared to the magnitudes of the already existing tagged moisture and the atmospheric transport conditions. Within the first hour of the simulation, the τ_{Q_t} pattern spreads toward the south due to the northerly winds (see area S in Figure 5c). In addition, the north-south age gradient is pronounced. Comparatively, fresh total tagged moisture with a low age (<0.3 h) is found over the northern part of the source area S since the atmosphere here contains a large

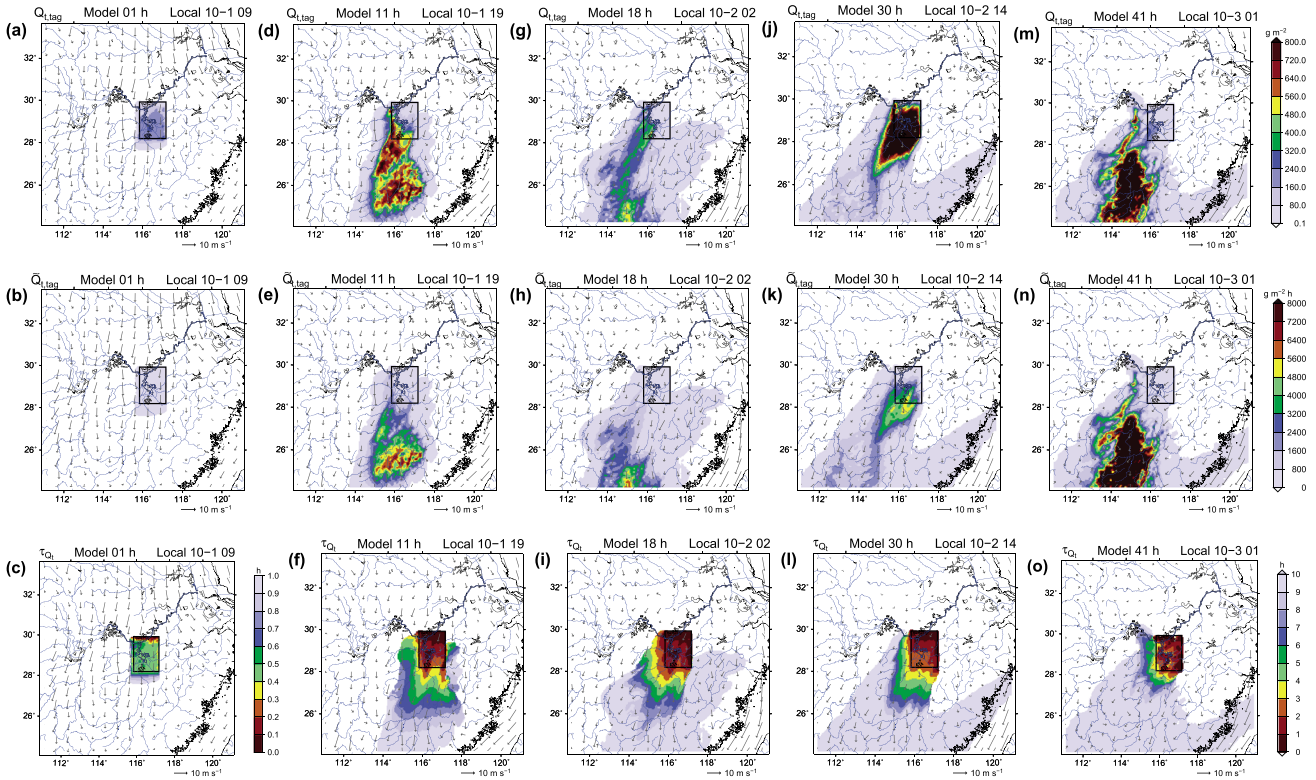

Figure 5. (a, d, g, j, and m) Horizontal distribution of column-integrated total tagged moisture $Q_{t,\mathrm{tag}}$ in g m^{-2}, (b, e, h, k, and n) column-integrated age-weighted total tagged moisture $\tilde{Q}_{t,\mathrm{tag}}$ in g m^{-2} h, and (c, f, i, l, and o) age τ_{Q_t} of column-integrated total tagged moisture in hours at different times during the first simulated 48 h (00:00 UTC 1 to 24:00 UTC 2) in October 2004. The source area S lies within the black rectangle.

proportion of newly tagged evaporated water. Over the southern part of the source area S, τ_{Q_t} is around 0.5 h (approximately the averaged age of the tagged moisture in the domain), attributed to the mixing between the newly and the already existing evaporated water. In contrast, the total tagged moisture over the area outside of area S but inside of area C has a mean age up to 0.96 h since there is less impact of fresh moisture advected from the source area S.

Figure 5f depicts the τ_{Q_t} pattern at the model time 11 h before a large amount of the older total tagged moisture starts to leave the area C (see Figure 5d). Tagged moisture more than 8 h old is also found over the adjacent part in the east and southeast of the source area S despite the small absolute values of the total tagged moisture, which may be mainly caused by repeated wind direction changes. Figures 5i, 5l, and 5o show age patterns on the second day at the selected three local times, consisting of early morning (Figure 5i), afternoon (Figure 5l), and night (Figure 5o). Due to gradually decreasing wind speed, the contoured age pattern with a large gradient tends now to be more centered on the source area S.

Figure 6 shows time series of hourly means of (Figure 6a) total tagged moisture, (Figure 6c) age-weighted total tagged moisture, and (Figure 6e) age of total tagged moisture, averaged over the analysis area C, and (Figures 6b, 6d, and 6f) the corresponding hourly net changes, during the first 48 h in October 2004. The tagged moisture content increases monotonically in the model atmosphere till 20:00 CST 1 October, decreases during the following evening and night, and increases again after sunrise on the next day (Figure 6a). The fluctuations reflect the comprehensive interactions among the daily cycles of evaporation, the formation of precipitation (to a lesser degree), the spatial redistribution due to various transport processes, and the loss due to outflow at lateral model boundaries. The trend of reduction of the total tagged moisture content (negative net change) during the nighttime follows the trend of enrichment (positive net change) during the daytime (Figure 6b). Within the first 12 h, the total tagged moisture nearly linearly increases, whereas the age-weighted tagged moisture shows a nonlinear increasing trend due to the age weighting process, with a nearly linear increment of the hourly net changes as time elapses (Figure 6d). Later in the evening, the age-weighted total tagged moisture switches from gain (positive change) to loss (negative change) (at 22:00 CST 1 in Figure 6d)

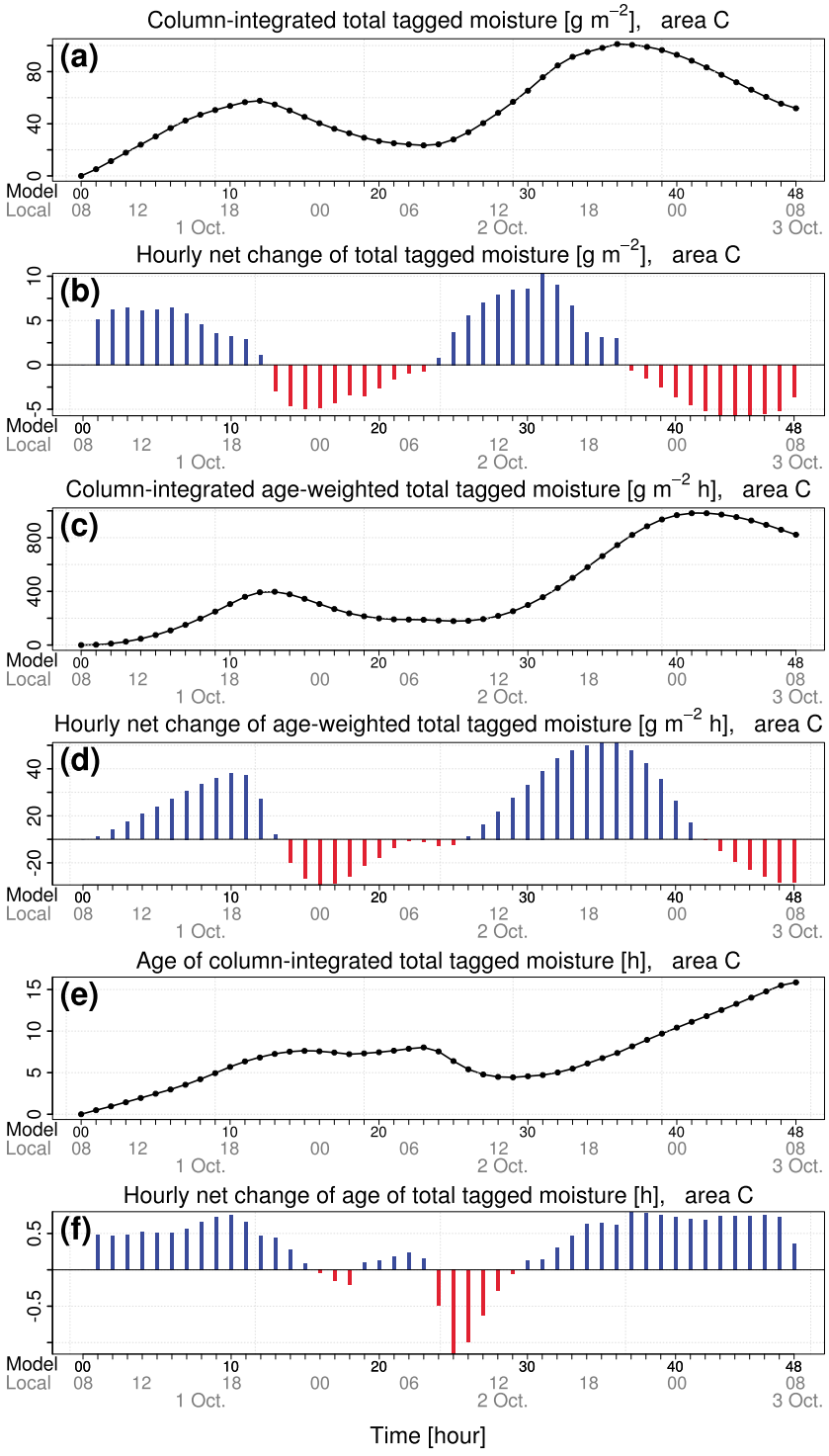

Figure 6. Time series from 08:00 CST 1 to 08:00 CST 3 in October 2004 of (a) column-integrated total tagged moisture $Q_{t,\mathrm{tag}}$ in g m^{-2}, (c) column-integrated age-weighted total tagged moisture $\tilde{Q}_{t,\mathrm{tag}}$ in g m^{-2} h, and (e) age τ_{Q_t} of column-integrated total tagged moisture in hours, and (b, d, and f) correspondingly hourly net changes, averaged over the analysis area C.

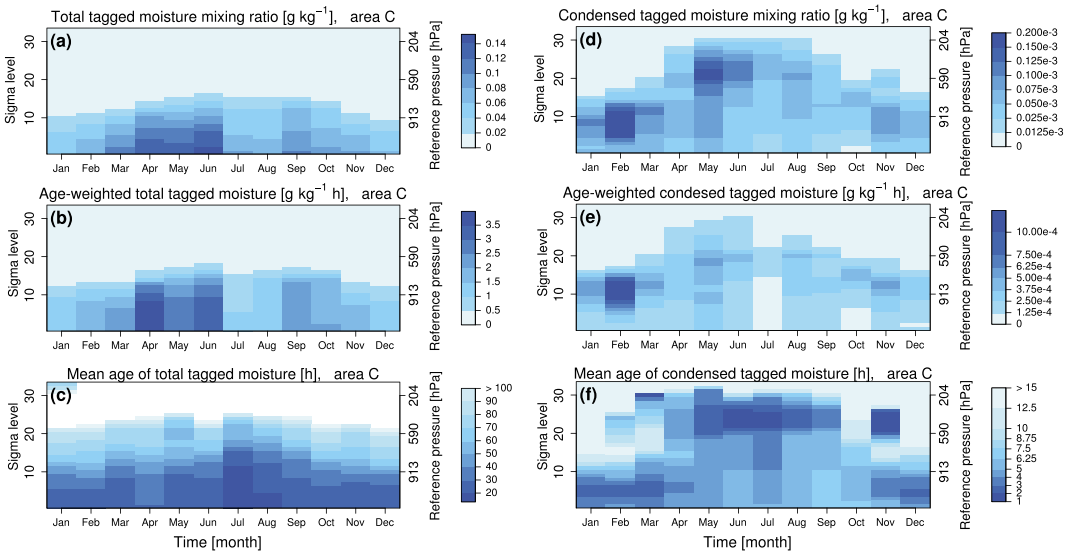

Figure 7. Time series of vertical distribution of (a) total tagged moisture mixing ratio $q_{t,\mathrm{tag}}$ in g kg^{-1}, (b) age-weighted total tagged moisture $\tilde{q}_{t,\mathrm{tag}}$ in g kg^{-1} h, and (c) mean age τ_{q_t} of total tagged moisture in hours, averaged over area C for each model layer and for each month in 2005. (d–f) The same as Figures 7a–7c but for condensed tagged moisture.

with a 1 h lag compared to the total tagged moisture (at 21:00 CST 1 in Figure 6d). The mean age (Figure 6e) of the total tagged moisture averaged over the analysis area C increases from 08:00 CST 1 until 19:00 CST 1 before large amounts of the total tagged moisture leaves the analysis area (see Figure 5d). In the first hours, the increase is nearly linear, after that it tends to be even stronger, since the weakening evaporation process (see Figure 6b) can only slightly refresh the large amount of the already existing (old) total tagged moisture within area C (see Figures 5e and 6d). In the following, the total tagged moisture becomes younger when the loss-induced decrease of the old total tagged moisture predominates, e.g., during the two periods (00:00–02:00, 08:00–13:00 CST 2).

4.3. Tagged Precipitation and Residence Times of Tagged Moisture

The atmospheric water residence times are now derived for the long-term run, i.e., the full year 2005. Figures 7a–7c show the vertical distribution of (a) the total tagged moisture $q_{t,\mathrm{tag}}$, (b) the age-weighted total tagged moisture $\tilde{q}_{t,\mathrm{tag}}$, and (c) the mean age of the total tagged moisture τ_{q_t} averaged over the analysis area C on monthly scales. Generally, the vertical profile of $\tilde{q}_{t,\mathrm{tag}}$ shows the same pattern as that of $q_{t,\mathrm{tag}}$: the values are dominated by the water vapor portion and are therefore high in the lower part of the atmosphere, especially during the rainy, warm season (April–June) (Figures 7a and 7b). The mean age of the total tagged moisture shown in Figure 7c varies from only 13 h near the surface, to around 60 h close to the planetary boundary layer top, to more than 110 h in the upper atmosphere (above around 590 hPa). In the boundary layer, the total tagged moisture in summer is younger (lower values of the mean age) than in winter, consistent with a generally faster atmospheric branch of the hydrological cycle in summer than in winter.

To examine the intensity of cloud and precipitation formation, monthly vertical profiles (d) of the *condensed* tagged moisture $q_{d,\mathrm{tag}}$ (i.e., the sum of tagged liquid and solid cloud and precipitation water), (e) of the age-weighted condensed tagged moisture $\tilde{q}_{d,\mathrm{tag}}$, and (f) of the corresponding mean age τ_{q_d} are shown in Figures 7d–7f. The vertical distribution of $q_{d,\mathrm{tag}}$ and $\tilde{q}_{d,\mathrm{tag}}$ shows significantly different from month to month. In winter, most of the condensed tagged water is formed in lower layers with a mean age of around 4 h, only a very small amount is found far above the boundary layer with a longer mean age, e.g., around 10 h in February and March. In contrast, in the rainy season and in the summer months, large-scale lifting and frequent convection result in a low age of $q_{d,\mathrm{tag}}$ (around 3 h) above the planetary boundary layer and in a higher age of $q_{d,\mathrm{tag}}$ (around 6 h) within the boundary layer. The different age profile in winter and summer indicates the diverse precipitation regimes. Moreover, the lower absolute values of the mean age of the condensed tagged moisture in summer than in winter suggest that the response of cloud and precipitating formation in summer is faster than in winter.

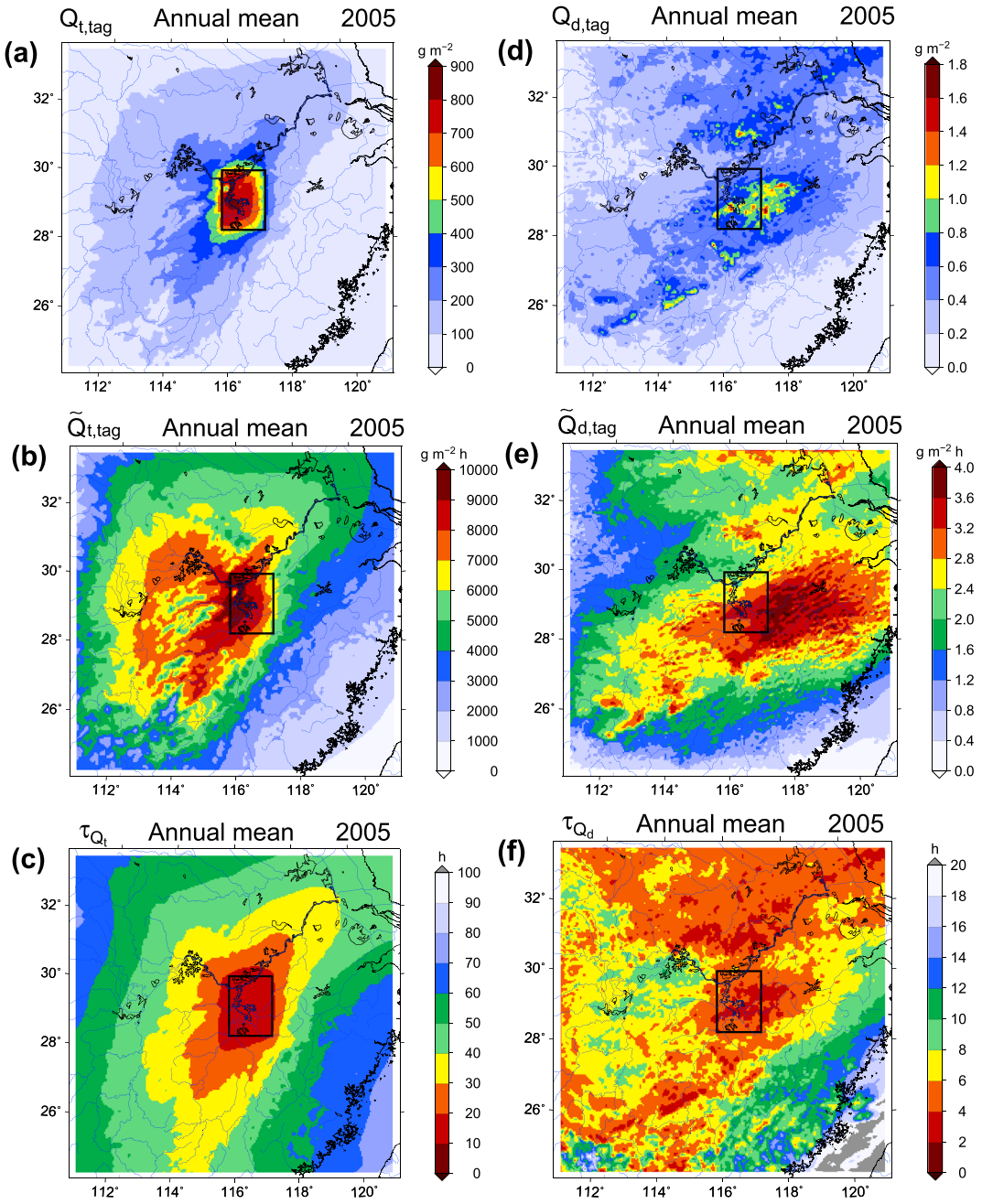

Figure 8. Annual mean of simulated column-integrated (a) total tagged moisture $Q_{t,tag}$ in g m^{-2}, (b) age-weighted total tagged moisture $\tilde{Q}_{t,tag}$ in g m^{-2} h, and (c) age τ_{Q_t} of total tagged moisture in hours, for the year 2005. (d–f) The same as Figures 8a–8c but for annual mean of simulated column-integrated condensed tagged moisture.

Figures 8a–8c show the horizontal distribution of (a) the column-integrated total tagged moisture $Q_{t,tag}$, (b) the column-integrated age-weighted total tagged moisture $\tilde{Q}_{t,tag}$, and (c) the corresponding age τ_{Q_t} averaged for 2005. Generally, the values of $Q_{t,tag}$ and $\tilde{Q}_{t,tag}$ decrease with distance from the source area with similar patterns. On the other hand, the age of the tagged moisture principally increases with increasing distance from the source area (Figure 8c). The values range from around 11 h over the source area S up to 90 h over the southeastern and northwestern corners of area C. Averaged over area C, the mean age of the total tagged moisture is around 36 h. Spatially, the northeast-southwest expanding pattern reflects the differently prevailing wind directions in the winter monsoon and summer monsoon-controlled seasons. Additionally, the gradient of the age toward the northwest is lower than that toward the southeast. It indicates that large amounts of total

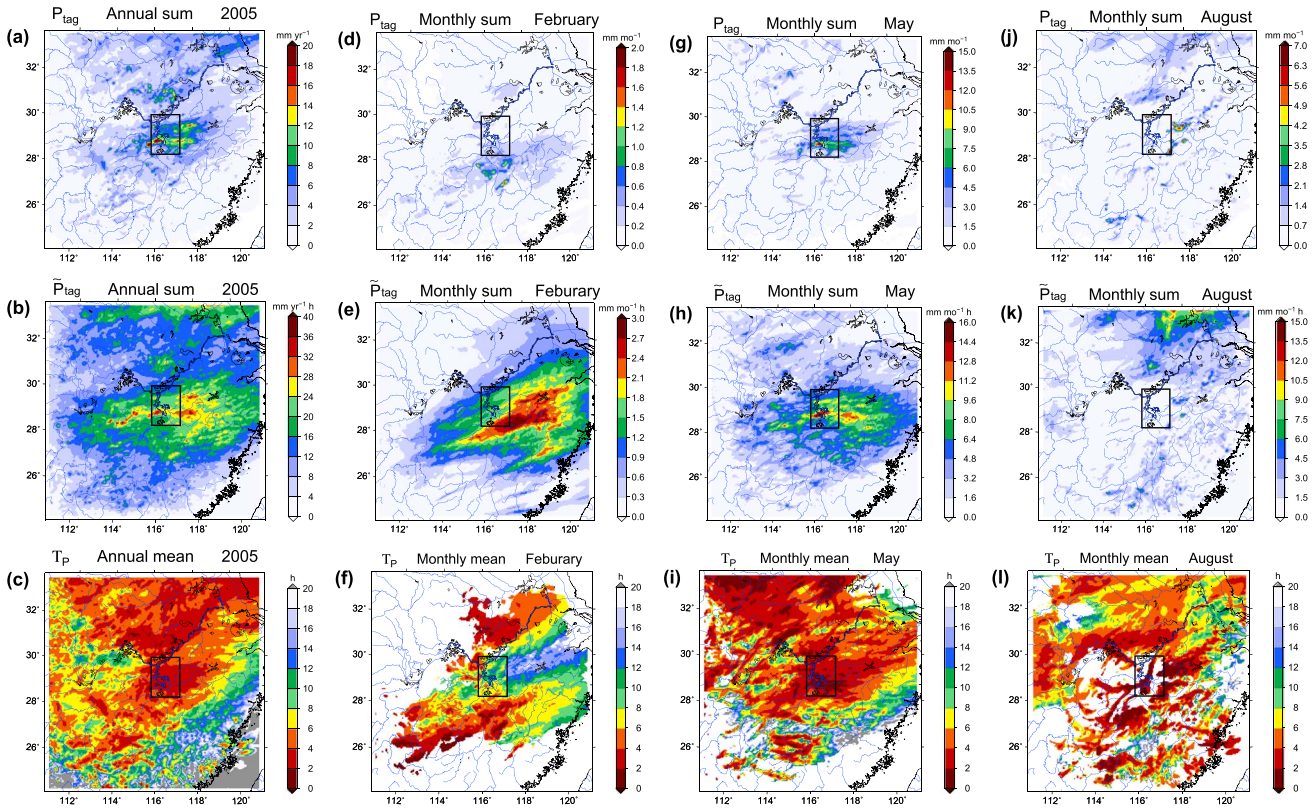

Figure 9. (a, d, g, and j) Sum of simulated tagged precipitation P_{tag} in mm yr^{-1} or mm mo^{-1}, (b, e, h, and k) age-weighted tagged precipitation $\tilde{P}_{tag}$ in mm yr^{-1} h or mm mo^{-1} h, and (c, f, i, and l) age T_P in hours for the whole year 2005 and for three selected months (February, May, and August).

tagged moisture are transported with strong southeasterly winds in summer, while small amounts of the older tagged moisture are transported with weak northwesterly winds in winter.

Figures 8d–8f show the horizontal distributions for the condensed parts. The horizontal distribution of the column-integrated age-weighted condensed tagged moisture $\tilde{Q}_{d,tag}$ (Figure 8e) generally follows the distribution of $Q_{d,tag}$ (Figure 8d). In comparison to the patterns for the total tagged moisture (see Figure 8c), the age patterns of the condensed part (Figure 8f) are distinctly different and the values are much lower (area mean: around 8 h). Moreover, the comparison between Figures 8d and 8f shows that, generally, larger values of the condensed tagged moisture correspond with lower ages in the atmosphere.

Figure 9 shows the spatial distribution of the simulated tagged precipitation P_{tag} (Figures 9a, 9d, 9g, and 9j), and the age-weighted tagged precipitation $\tilde{P}_{tag}$ (Figures 9b, 9e, 9h, and 9k) for the total year 2005 and three selected months (February, May, and August). The patterns of the age T_P are depicted as well (Figures 9c, 9f, 9i, and 9l). Accumulated over the year 2005, the horizontal distribution of the tagged precipitation patterns P_{tag} (Figure 9a) is closely related to the condensed tagged moisture patterns $Q_{d,tag}$ (Figure 8d). Similarly, the age-weighted tagged precipitation distribution $\tilde{P}_{tag}$ in Figure 9b appears like the distribution of $\tilde{Q}_{d,tag}$ (see Figure 8e). Figure 9c shows the age patterns synthesizing the variations of evaporation, atmospheric transport conditions, and precipitating events for the whole year 2005. Overall, age is negatively correlated with the tagged precipitation. Most of the young age ($\lesssim$ 3 h) are found in regions where relatively large amounts of the tagged precipitation ($\gtrsim$ 8 mm yr^{-1}) occur, for example, in the source area S and in the north along the Yangtze River Valley. The reason is, that summer precipitation accounts for a large proportion of the annual tagged precipitation in these regions (e.g., May in Figure 9g and August in Figure 9j), due to the comparatively faster response of the atmospheric branch of the hydrological cycle. In contrast, significantly decreasing wind speed and rapidly changing wind direction in winter and in the transient seasons lead to longer atmospheric water pathways of the tagged moisture before precipitating, for example, in the southeast quadrant. It is worth to note that the age patterns of the tagged precipitation over the land surface (Figure 9c) is very similar to the

age patterns of the condensed tagged moisture in the atmosphere but are 1 h shorter (Figure 8f). This time lag is probably ascribed to a longer life of the nonprecipitating and later reevaporating condensed moisture.

Next, we consider the selected 3 months (February, May, and August) in 2005 to reveal the impact of the different monsoon-controlled precipitation regimes on the monthly variations of the age-weighted tagged precipitation patterns and of the corresponding age patterns. In February, the prevailing northwesterly winds generate a band-like structure of the age-weighted tagged precipitation $\tilde{P}_{tag}$ (Figure 9e). The maximum values of $\tilde{P}_{tag}$ are located in the adjacent parts to the east and to the southeast of the source area. The tagged precipitation P_{tag} with large values generally has a lower age T_P, while comparatively high (around 8 h) age is found for relatively low values of P_{tag} (around 0.4 mm mo^{-1}) (see Figures 9d and 9f). Regions with both significantly high age (> 12 h) and very small amount of tagged precipitation (<0.2 mm mo^{-1}) are found in the east of the source area S, probably due to the repeated changes in wind direction. In the rainy season, like in May, the age-weighted tagged precipitation (Figure 9h) has higher values than in February (see Figure 9e) and the patterns are generally similar to the patterns of the tagged precipitation (Figure 9g), with maximum values in the source area S and its surrounding regions. Correspondingly, the age in these regions shown in Figure 9i is low (< 5 h), since large amounts of the tagged moisture is involved in fast, large-scale precipitation processes (see Figure 7). A low age of the tagged precipitation is also found in the northeast and in the south, where the tagged moisture originating from the source area S is transported by strong winds and then precipitates in accordance with locally convective events. In August, some large values of the tagged precipitation P_{tag} (Figure 9g) and of the age-weighted tagged precipitation $\tilde{P}_{tag}$ (Figure 9h) are found in various regions in and around the source area S. However, regions with maximum age-weighted tagged precipitation (> 10 mm mo^{-1} h) are in the remote north (Figure 9h) with a long time residing in the atmosphere (Figure 9l) due to the decreasing strength of the summer monsoon and the changing wind directions associated with the retreat of the monsoon.

Overall, our results clearly depict the significant seasonal cycles and the different (i.e., vertical and horizontal) patterns of the tagged precipitation and the accompanying age. These reveal the dynamical complexity of the atmospheric branch of the hydrological cycle under varying meteorological conditions.

4.4. Residence Times Corresponding to Partitioned Direct Evaporation and Transpiration

In the context of E-Tagging partitioning (see section 2.1), the atmospheric residence times of the transpired water and of the direct evaporated water are separately calculated in two long-term simulations and are presented here by considering seasonal and spatial variability.

Time series of monthly mean of moisture content (Figures10a and 10c) and of age (Figures 10b and 10d) for the year 2005 are displayed in Figure 10. The tagged moisture $Q_{t,\mathrm{tag}E_d}$ due to direct evaporation (Figure 10a) significantly increases from January to March reaches its maximum during the months from April to June and becomes relatively low (around 60 g m^{-2}) in the following months. In contrast, the tagged moisture $Q_{t,\mathrm{tag}E_t}$ due to transpiration has low values in winter and reaches its maximum values in June and September. This reveals that in the summer season, the transpiration turns more important for the formation of tagged moisture and also for the formation of tagged precipitation [*Wei et al.*, 2015]. This result is generally in line with a recent water isotopes study for a humid subtropical rice paddy field that found that transpiration dominates total evaporation in the atmospheric boundary layer in summer but not in winter [*Wei et al.*, 2016]. It is worth to note that due to the nonnegligible effects (e.g., the isotope amount effect) on isotopic composition of precipitation there were still large uncertainties in their estimates and that our process-based approach including a sophisticated land surface model can help to clarify and narrow down uncertainties. Considering the mean age (Figure 10b), generally, there is a comparatively small difference between in the ages of $Q_{t,\mathrm{tag}E_d}$ and of $Q_{t,\mathrm{tag}E_t}$. The difference is ascribed to different timescales of land surface transpiration and direct evaporation response [*Scott et al.*, 1997; *Lohmann and Wood*, 2003], which was discussed in the recent study of *van der Ent et al.* [2014] as well. As a result, the low values of differences (≤ 4 h) between the ages of $Q_{t,\mathrm{tag}E_d}$ and of $Q_{t,\mathrm{tag}E_t}$ are found from January to June ($\tau_{Q_{t,E_d}} > \tau_{Q_{t,E_t}}$) and the relatively higher values (≥ 5 h) for the period from October to December ($\tau_{Q_{t,E_d}} < \tau_{Q_{t,E_t}}$). The age of $Q_{t,\mathrm{tag}E_t}$ reaches nearly the same low value as that of $Q_{t,\mathrm{tag}E_d}$ during the dry period from July to September, which is likely due to the stronger effect of the transpired water uptake by vegetation and the less supply of directly evaporated water from the dry top soil layer.

In comparison with the absolute value of the area-averaged column-integrated total tagged moisture (Figure 10a), the condensed amount for the two partitions ($Q_{d,\mathrm{tag}E_d}$ and $Q_{d,\mathrm{tag}E_t}$) is nearly 2 orders of magnitude lower (Figure 10c). Generally, the monthly variation of $Q_{d,\mathrm{tag}E_d}$ is similar to the variation of $Q_{d,\mathrm{tag}E_t}$.

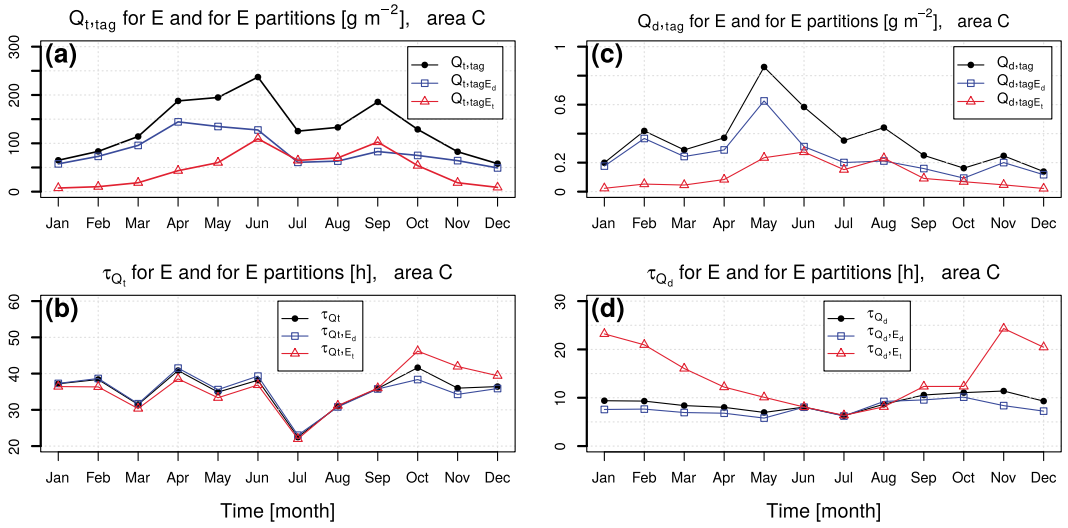

Figure 10. Time series of monthly mean of column-integrated (a) total tagged moisture $Q_{t,\mathrm{tag}}$ in g m^{-2} and (b) age of total tagged moisture τ_{Q_t} in hours, originating from total evaporated water (in black), from direct evaporated water (in blue), and from transpired water (in red), each averaged over area C. (c, d) The same as the Figures 10a and 10b but for condensed tagged moisture.

But the respective maximum values are found in different months: in May for $Q_{d,\mathrm{tag}E_d}$ and in June and August for $Q_{d,\mathrm{tag}E_t}$. Correspondingly, averaged over area C, the monthly variation of the mean age of column-integrated $Q_{d,\mathrm{tag}E_t}$ (Figure 10d) is larger (from 7 h in July to 25 h in November) compared with that of $Q_{d,\mathrm{tag}E_d}$ (from 5 to 10 h). The mean age of $Q_{d,\mathrm{tag}E_d}$ is lower than that of $Q_{t,\mathrm{tag}E_t}$, especially in the cold season with the difference of around 15 h, since the direct evaporation is dominant for the formation of the condensed moisture during this period. This difference becomes small in the transient season and even nearly no difference is found during the warm and dry months from June to August. It indicates that averaged over area C, the column-integrated transpired and direct evaporated water nearly have the same probability to be involved in forming clouds and tagged precipitation during the above-discussed warm and dry months.

Figures 11a and 11b show the vertical profiles of the annual mean of the total tagged moisture mixing ratio and its mean age for total evaporation E and for its partitions E_d and E_t, averaged over area C for 2005. Overall, the values of the total tagged moisture decrease with increasing height and reaching values near zero above the planetary boundary layer (Figure 11a). In all layers, the contribution by direct evaporation dominates, which differs from recent studies, which found that transpiration dominates terrestrial water fluxes [*Jasechko et al.*, 2013; *Schlesinger and Jasechko*, 2014; *van der Ent et al.*, 2014; *Wang-Erlandsson et al.*, 2014]. The different representations of land surface characteristics of the source areas in our and in other recent studies [e.g., *van der Ent et al.*, 2014] are the main reason [*Wei et al.*, 2015]. Our moisture source area contains a large fraction of moist land use types (water body and wetlands) with direct evaporation. These conditions allow the process transfer of standing water at or near the surface over a much broader area, particularly during rainfall events, in comparison to transpiration of water from the root zone [*Jasechko et al.*, 2013]. Since the dominant land cover type of the continent is plant, there is no doubt that the continent as a source area provides more transpiration than direct evaporation [*Good et al.*, 2015]. Therefore, the land surface characteristics play an important role in the regional atmospheric part of hydrological cycle [*van der Ent et al.*, 2014; *Wei et al.*, 2015].

Both the total tagged moisture for transpiration and for direct evaporation have short residence times near the surface and longer residence times in the upper part of the atmosphere (Figure 11b). Below around 950 hPa (seventh sigma level), the age for direct evaporation is lower than that for transpiration. The reason is probably that a large amount of direct evaporated moisture originates during the wet period frequently coinciding with convection. Instead, the transpired moisture originates more continuously (with continuous, we express the diurnal cycles of the transpiration signal and distinguish from intermittent direct evaporation) during both wet and dry period and shows higher mean age, especially contributed by the long residence times of water transpired during the dry period. In contrast, an inversed difference in the profiles of the mean age for transpiration (younger) and direct evaporation (older) is found in the upper part of the atmosphere

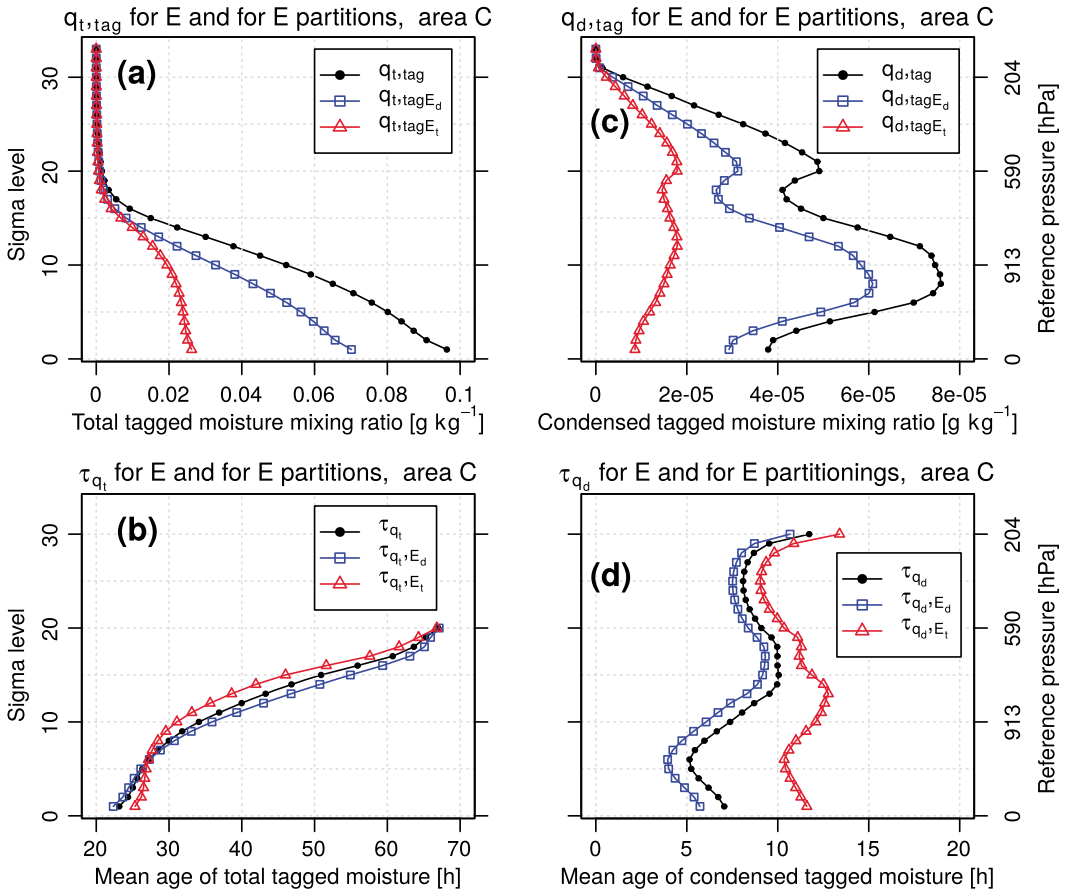

Figure 11. Vertical distribution of annual mean of (a) total tagged moisture mixing ratio $q_{t,tag}$ in g kg^{-1}, (b) mean age of total tagged moisture mixing ratio τ_{q_t} in hours, originating from total evaporated water (in black), from direct evaporated water (in blue), and from transpired water (in red), averaged over area C for the year 2005. (c, d) The right column shows the same as the left column but for condensed tagged moisture.

(above the seventh sigma level). This inversion is presumably ascribed to the transpired water uptake from the wet root zone contrasting to less direct evaporated water from the dry top soil, especially during the dry season frequently involved in convection. This explanation is generally supported by *van der Ent et al.* [2014]. Overall, these differences reflect the different features of the respective processes: intermittent direct evaporation, more continuous transpiration, and rising and mixing of the two partitions.

Figures 11c and 11d show the same as Figures 11a and 11b except for the condensed tagged moisture. Two peaks of the condensed tagged moisture mixing ratio for the two E partitions are found (Figure 11c), which indicate the overall meteorological conditions relating to the atmospheric circulations over Southeast China. One peak is found around 913 hPa (tenth sigma level), presumably due to the mean stratification, mainly in winter. Another peak around 590 hPa (twentieth sigma level) may be caused by convection dominating in summer. In all layers, the condensed tagged moisture $q_{d,\mathrm{tag}}$ is mainly contributed by the younger direct evaporation. The mean age of $q_{d,\mathrm{tag}}$ for direct evaporation near the surface is lower than in the upper part of the atmosphere, which is inversed for transpiration (Figure 11d). We attribute this result to the different involved convection and precipitation regimes (i.e., wet and dry weather conditions) and in turns the different response timescales of transpiration and of direct evaporation. In winter over area C, the condensed tagged moisture is predominantly formed near the land surface. During this period, the dominant direct evaporation flux can be involved in forming cloud and precipitation more frequently than the very small amount of transpiration flux (see Figures 10c and 10d). During the rainy season (e.g., May), the condensed tagged moisture is found both near the surface and in the upper part of the atmosphere due to large-scale convection. Since transpiration is less effective for water from the root zone than direct evaporation for water near or at the moist land surface, the portion of newly transpired water in the atmosphere is smaller than that of newly directly

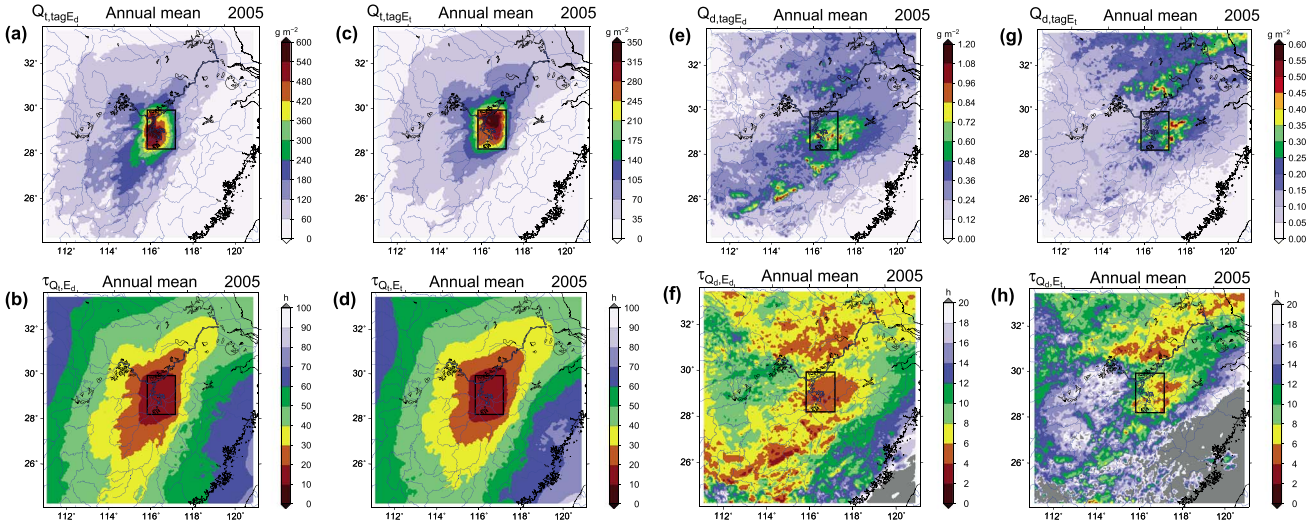

Figure 12. Annual mean of simulated column-integrated (a) tagged moisture originating from direct evaporated water $Q_{t,tagE_d}$ in g m^{-2} and (b) age τ_{Q_t,E_d} of tagged moisture from direct evaporation in hours, averaged for the year 2005. (c, d) The same as Figures 12a and 12b but for tagged moisture from transpiration. (e) Annual mean of condensed tagged moisture from direct evaporation $Q_{d,tagE_d}$ in g m^{-2} and (f) corresponding age τ_{Q_d,E_d} in hours. (g, h) The same as Figures 12e and 12f but for transpiration.

evaporated water. In turn, transpired water has relatively lower chance than directly evaporated water to be involved in the formation of clouds and precipitation systems, even under the condition of frequent convection. As a result, the age of directly evaporated water is younger, due to the effective input of the newly tagged directly evaporated water, than the age of transpired water, due to the delay input of the newly tagged transpired water. By contrast, during comparatively warm and dry months (from June to August), the contribution of transpiration to total evaporation reaches its maximum (around 50%). Under the condition of dry top soil and the wet root zone, the relatively large amount of newly transpired water can have the nearly same efficiency as the directly evaporated water to be lifted up to form the cloud and precipitation. For example, in July, around the 15th model layer, the atmospheric residence time of the area-averaged condensed tagged moisture for transpiration is even shorter than that for direct evaporation (not shown here). Therefore, the condensed tagged moisture for transpiration has shorter atmospheric times in the upper part of the atmosphere than near the surface. Moreover, the difference of the residence times of the condensed tagged moisture for transpiration and for direct evaporation in the upper part of the atmosphere is smaller than that near the surface. Overall, the result reveals that the direct evaporated water contributes to the formation of clouds and precipitation more near the land surface in the cold and wet months, while the transpired moisture condenses relatively more and later in the upper part of the atmosphere in warm and dry months. By comparing the mean age profiles of $q_{d,tag}$ for the two E partitions for the whole year 2005, the atmosphere has a quick response to the direct evaporation process and a slower response to the transpiration process.

Horizontally, the pattern of the tagged moisture originating from direct evaporation $Q_{t,tagE_d}$ (Figure 12a) follows the pattern of the total tagged moisture from total evaporation $Q_{t,tag}$ (see Figure 8a). Averaged over area C, $Q_{t,tagE_d}$ accounts for 64% of $Q_{t,tag}$. The age pattern of $Q_{t,tagE_d}$ (Figure 12b) is similar to the age pattern of $Q_{t,tag}$ (Figure 8c). Compared with the $Q_{t,tagE_d}$ pattern, the pattern for the transpiration contribution is shifted slightly toward the north (Figure 12c). Especially, over the southwestern part of area C the atmosphere contains younger (around 40 h) tagged moisture contributed by direct evaporation and slightly older (around 50 h) moisture by transpiration. Such a difference is also found in the southeast quadrant, while over the northern and western parts, the mean age for direct evaporation and for transpiration shows similar values. Averaged over area C, the mean age of $Q_{t,tagE_d}$ and $Q_{t,tagE_t}$ are nearly equal to the value for total evaporation τ_{Q_t}, i.e., 36 h.

Regarding the condensed tagged moisture $Q_{d,tag}$, 69.2% is contributed by direct evaporation and the rest by transpiration. The area-averaged age of $Q_{t,tagE_d}$ (around 7 h) is lower than that of $Q_{t,tagE_t}$ (around 11 h). A large amount of the condensed tagged moisture $Q_{d,tagE_d}$ originating from direct evaporated water is found in the atmosphere over the source area S and in the adjacent part to the east and in the south (Figure 12e), with an

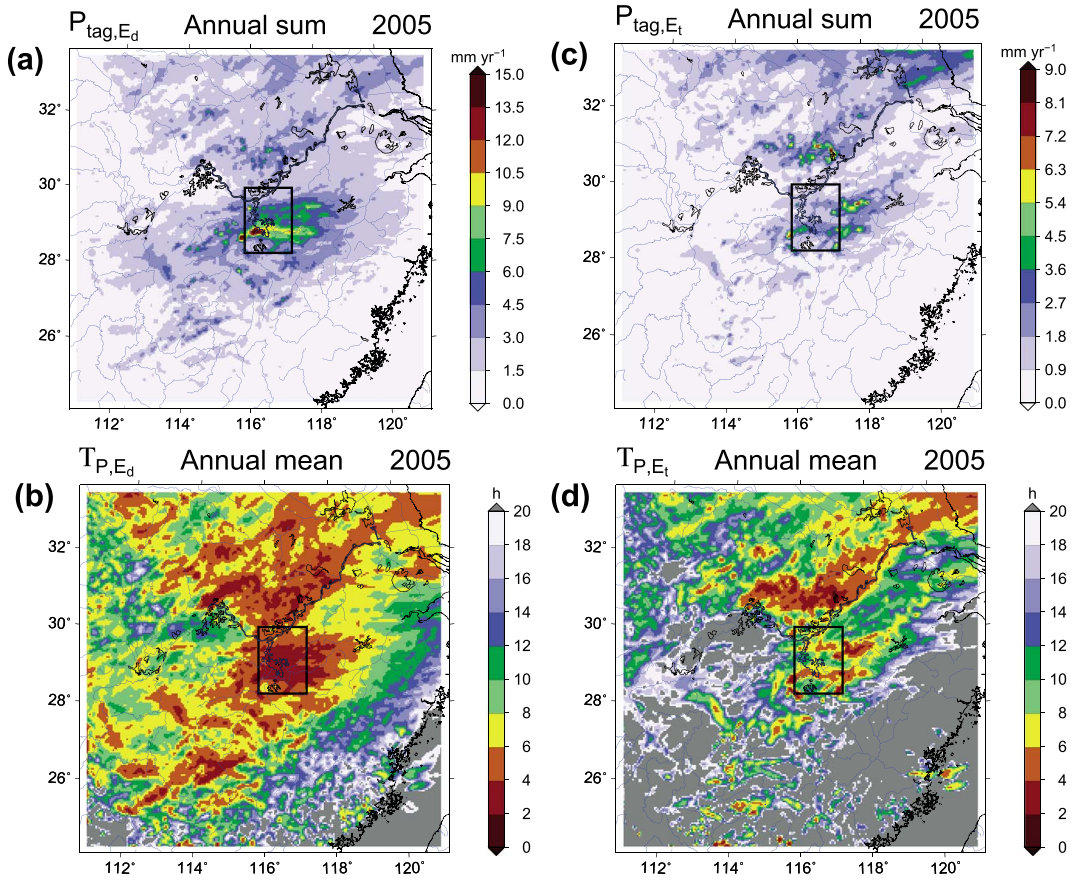

Figure 13. (a) Annual sum of simulated tagged precipitation originating from direct evaporation P_{tag,E_d} in mm yr^{-1} and (b) corresponding mean age T_{P,E_d} in hours, for the year 2005. (c, d) The same as the Figures 13a and 13b but for transpiration.

age of more than 6 h (Figure 12f). In contrast, transpired water is more important over the regions close to the source area S and in the north (Figure 12g), with an age of less than 6 h (Figure 12h). In comparison, in the south, the direct evaporated water contributes nearly to all the condensed tagged moisture with low age (<8 h), whereas the transpired water contributes little with higher age (> 12 h). In the north, the two E partitions contribute nearly equally with similar age (only ≤ 2 h lag between the direct evaporated precipitation and the transpired precipitation).

Figures 13a and 13c show the horizontal distribution of the tagged precipitation contributed by the two E partitions, accumulated for the year 2005. The annual mean of the corresponding age is shown in Figure 13b and 13d. Generally, the patterns of the partitioned tagged precipitation are similar to the patterns of the partitioned condensed tagged moisture (see Figures 12e and 12g). The same holds for their age patterns (Figures 13b and 13d compared with Figures 12f and 12h). The direct evaporation contributes more to the total tagged precipitation with a lower age (area mean: 6.6 h) than the transpiration (area mean: 10.7 h). Over the regions around the source area and in the north, the ages of the two partitioned tagged precipitation are similarly short (<6 h). However, in the west and in the south, the tagged precipitation by transpiration has much higher age than that by direct evaporation.

5. Summary and Conclusions

In this study, an age-weighted evaporation tagging partitioning algorithm implemented in the regional climate model MM5 was applied. This algorithm is fully three-dimensional and considers all water transport and phase transition processes. Using this extended model as a diagnostic tool, the moisture transpired and directly evaporated from a given source area can be separately tagged and then tracked across the atmosphere until it returns to the land surface as precipitation or leaves the model domain. Additionally, the age

weighting mechanism, calculating the atmospheric residence times of the direct evaporated and transpired water, allows assessment of the speed of the response of the atmospheric branch of the hydrological cycle.

Our results show that the rates by which evaporated moisture returns to the surface via precipitation (i.e., the speed of the atmospheric branch of the hydrological cycle) changes seasonally and spatially. Temporal and spatial variations of the mean age of the tagged moisture in the Poyang Lake region in Southeast China are controlled by the magnitudes of the tagged newly evaporated water compared to the magnitudes of the already existing older tagged moisture and by changes in the atmospheric transport conditions.

Different moisture components (i.e., total moisture, condensed moisture, and precipitation) exhibit different temporal and spatial variability of the atmospheric residence times. The column-integrated atmospheric total tagged moisture originating from the Poyang Lake region has a comparatively long residence time in winter and a shorter time in summer. Spatially, the age of the total tagged moisture increases with the length of the moisture pathways, resulting in most cases of increasing distance to the Poyang Lake region as well. The horizontal and vertical age patterns of the total tagged moisture reflect differently prevailing wind directions and speeds in the winter and summer monsoon-controlled seasons.

Regarding the cloud and precipitation formation, most of the condensed tagged moisture with short residence times is found in winter near the land surface and in summer in the higher layers of the atmosphere, which reflects the varying atmospheric stability conditions and the different precipitation regimes in Southeast China. For the entire year 2005, the age of the condensed tagged moisture, i.e., around 8 h averaged over area C (nearly Southeast China), is much shorter in comparison with that of the total tagged moisture (area mean around 36 h). The tagged precipitation has different age patterns from month to month, which reveals the varying conditions impacted by the East Asian monsoon and the dynamical complexity of the atmospheric branch of the hydrological cycle. In comparison, the annual mean age patterns of the tagged precipitation over the land surface is very similar to the annual mean age patterns of the condensed tagged moisture in the atmosphere but being around 1 h shorter. A longer life of the nonprecipitating and later reevaporating condensed moisture presumably accounts for this time lag.

Regarding the different moisture sources, the atmospheric residence times of transpired moisture significantly differ from that of directly evaporated moisture. Considering the annual mean age profiles, the age of the total tagged moisture for direct evaporation is lower than that for transpiration near the surface and the inversed case is found in higher layers of the atmosphere. This phenomenon reflects different features of respective process over the land surface: intermittent direct evaporation, more continuous transpiration, and mixing of the two E partitions. However, the area-averaged condensed tagged moisture for transpiration always has higher age than that for direct evaporation in all vertical layers of the atmosphere.

Considering the annual mean age patterns, over the southwestern part of area C and in the southeast quadrant, the atmosphere contains the "fresh" (around 40 h) total tagged moisture contributed by direct evaporation and "older" (around 50 h) by transpiration. Over the northern and western parts, the age for the two E partitions reaches similar values. On the monthly scale averaged over area C, there is no significant difference between the age of the total tagged moisture for the two E partitions. Integrated over all vertical layers of the atmosphere in 2005 a large amount of the condensed tagged moisture by direct evaporation with lower age is found in the south, while the two E partitions play nearly the same role in forming the cloud and precipitation in the north. Monthly, the age of the column-integrated, area-averaged condensed tagged moisture due to direct evaporation is lower than the age due to transpiration, especially in the cold season. This age difference becomes smaller in the transient season and even no difference during the warm months from June to August.

We summarize our main results as follows: for the whole year 2005, integrated over all layers of the atmosphere and averaged over area C, 11% of direct evaporated water (10% of transpired water) precipitates locally and the rest leaves the model domain. The direct evaporated water accounts for 64% of the total tagged moisture and the transpired water for 36% with a mean age of around 36 h for both. Regarding the condensed tagged moisture, 69.2% originates from the direct evaporated water and 30.8% from the transpired water, with a mean age of 7 h and 11 h, respectively. Similarly, the annual-aggregated, area-averaged tagged precipitation consists of a large proportion (69%) of direct evaporated water with comparatively short atmospheric residence times (area mean: 6.6 h) and of a small amount of transpired water with longer atmospheric residence times (area mean: 10.7 h).

Studies using isotopes methods [e.g., *Jasechko et al.*, 2013; *Schlesinger and Jasechko*, 2014; *Evaristo et al.*, 2015; *Good et al.*, 2015] found transpiration contributions to total evaporation ranging from 35% to 90%. In our study, on average, the contribution of transpiration to atmospheric water is relatively low. The different contribution ratios are mainly ascribed to the different representations of the moisture source areas, which emphasizes the crucial role of land surface characteristics [*Wei et al.*, 2015]. A recent study about water isotopes [*Wei et al.*, 2016] showed that transpiration dominates the total evaporation over a paddy rice area in the period in summer, but not in winter. Our regional numerical study is generally in agreement with the study of *Wei et al.* [2016]. However, it should be noted that there are still considerable uncertainties in transpiration estimates, as, e.g., reported by *Coenders-Gerrits et al.* [2014]. Our process-based approach has the potential to help to reduce these uncertainties. Moreover, this model study confirms previous findings that vegetation cover and land use are of important to the atmospheric hydrological cycle, particularly during the dry season [*Kunstmann and Jung*, 2007; *Wang-Erlandsson et al.*, 2014; *van der Ent et al.*, 2014]. As shown by *Scott et al.* [1997] in a global analytic analysis, the timescales of transpiration differ from that of direct evaporation. A global moisture recycling study by *van der Ent et al.* [2014] found that transpiration resides in the atmosphere longer than direct evaporation.

In conclusion, the information on the timescales for the atmospheric branch of the hydrological cycle, particularly for transpired and evaporated water, has been explicitly quantified by using our age-weighted regional E-Tagging approach. Significant difference in atmospheric residence times of transpired moisture and of directly evaporated moisture until falling out as precipitation indicates different underlying mechanisms controlling interactions between the land surface and the atmosphere, which are still not fully understood. Our study suggests that the complexity of the atmospheric branch of the hydrological cycle, including the impact of the land surface characteristics, should be taken into account for assessment of the atmospheric water residence times and for a better understanding of land-atmosphere interaction mechanisms.

Our newly developed age-weighted regional evaporation tagging approach is generally enough to be employed for further studies worldwide on climate change impacts due to land use and land cover changes. Following this methodological approach, future research can also address how atmospheric water residence times change regionally under global warming.

Acknowledgments

This work is funded by China Scholarship Council (CSC). The authors would like to thank the following data sources: European Centre for Medium-Range Weather Forecasts *ERA-Interim* (http://apps.ecmwf.int/datasets/), APHRODITE's Water Resources *APHRODITE* (http://www.chikyu.ac.jp/precip/), NOAA/National Centers for Environmental Information *IGRA* (https://www.ncdc.noaa.gov/data-access/weather-balloon/integrated-global-radiosonde-archive). We thank Benjamin Fersch (KIT/IMK-IFU), Joël Arnault (KIT/IMK-IFU), and Christof Lorenz (KIT/IMK-IFU) for their valuable scientific discussions. The authors would also like to thank Youngsun Kim (KIT/IMK-IFU) and Dominikus Heinzeller (KIT/IMK-IFU), who improved the quality of our manuscript with their valuable comments and corrections. We would like to to thank two anonymous reviewers for detailed comments and suggestions that helped to improve our manuscript.

References

Allen, M. R., and W. J. Ingram (2002), Constraints on future changes in climate and the hydrologic cycle, *Nature*, *419*(6903), 224–232, doi:10.1038/nature01092.

Arnault, J., R. Knoche, J. Wei, and H. Kunstmann (2016), Evaporation tagging and atmospehric water budget analysis with WRF: A regional precipitation recycling study for West Africa, *Water Resour. Res.*, *52*(3), 1544–1567, doi:10.1002/2015WR017704.

Bolin, B., and R. Henning (1973), A note on the concepts of age distribution and transit time in natural reservoirs, *Tellus*, *25*(1), 58–62, doi:10.1111/j.2153-3490.1973.tb01594.x.

Chen, F., and J. Dudhia (2001), Coupling an advanced land surface-hydrology model with the Penn State-NCAR MM5 modeling system. Part I: Model implementation and sensitivity, *Mon. Weather Rev.*, *129*(4), 569–585, doi:10.1175/1520-0493(2001)129<0569:CAALSH>2.0.CO;2.

Chow, K. C., H.-W. Tong, and J. C. L Chan (2008), Water vapor sources associated with 752 the early summer precipitation over China, *Clim. Dyn. 30*(5), 497–517, doi:10.1007/s00382-007-0301-6.

Coenders-Gerrits, A. M. J., R. J. van der Ent, T. A. Bogaard, L. Wang-Erlandsson, M. Hrachowitz, and H. H. G. Savenije (2014), Uncertainties in transpiration estimates, *Nature*, *506*, E1–E2, doi:10.1038/nature12925.

Ding, Y., and J. C. L. Chan (2005), The East Asian summer monsoon: An overview, *Meteorol. Atmos. Phys.*, *89*(1–4), 117–142, doi:10.1007/s00703-005-0125-z.

Dudhia, J. (1989), Numerical study of convection observed during the winter monsoon experiment using a mesoscale two-dimensional model, *J. Atmos. Sci.*, *46*(20), 3077–3107, doi:10.1175/1520-0469(1989)046<3077:NSOCOD>2.0.CO;2.

Dudhia, J. (1993), A nonhydrostatic version of the Penn State-NCAR mesoscale model: Validation tests and simulation of an Atlantic cyclone and cold front, *Mon. Weather Rev.*, *121*(5), 1493–1513, doi:10.1175/1520-0493(1993)121<1493:ANVOTP>2.0.CO;2.

Durre, I., R. S. Vose, and D. B. Wuertz (2006), Overview of the integrated global radiosonde archive, *J. Clim.*, *19*(1), 53–68, doi:10.1175/JCLI3594.1.

Durre, I., R. S. Vose, and D. B. Wuertz (2008), Robust automated quality assurance of radiosonde temperatures, *J. Appl. Meteorol. Climatol.*, *47*(8), 2081–2095, doi:10.1175/2008JAMC1809.1.

Evaristo, J., S. Jasechko, and J. J. McDonnell (2015), Global separation of plant transpiration from groundwater and streamflow, *Nature*, *525*, 91–94, doi:10.1038/nature14983.

Feng, L., C. Hu, X. Chen, X. Cai, L. Tian, and W. Gan (2012), Assessment of inundation changes of Poyang Lake using MODIS observations between 2000 and 2010, *Remote Sens. Environ.*, *121*, 80–92, doi:10.1016/j.rse.2012.01.014.

Goessling, H. F., and C. H. Reick (2013), On the "well-mixed" assumption and numerical 2-D tracing of atmospheric moisture, *Atmos. Chem. Phys.*, *13*(11), 5567–5585, doi:10.5194/acp-13-5567-2013.

Gomez, J. D., and J. L. Wilson (2013), Age distributions and dynamically changing hydrologic systems: Exploring topography-driven flow, *Water Resour. Res.*, *49*(3), 1503–1522, doi:10.1002/wrcr.20127.

Good, P. S., D. Noone, and G. Bowen (2015), Hydrologic connectivity constrains partitioning of global terrestrial water fluxes, *Science*, *349*(6244), 175–177, doi:10.1126/science.aaa5931.

Grell, A. G., J. Dudhia, and R. D. Stauffer (1994), A description of the fifth-generation Penn State/NCAR mesoscale model (MM5), *Tech. Rep., NCAR Technical Note NCAR/TN-398+STR*, Boulder, Colo.

Harman, C. J., and M. Kim (2014), An efficient tracer test for time-variable transit time distributions in periodic hydrodynamic systems, *Geophys. Res. Lett.*, *41*(5), 1567–1575, doi:10.1002/2013GL058980.

Held, I. M., and B. J. Soden (2006), Robust responses of the hydrological cycle to global warming, *J. Clim.*, *19*(21), 5686–5699, doi:10.1175/JCLI3990.1.

Hong, S.-Y., and H.-L. Pan (1996), Nonlocal boundary layer vertical diffusion in a medium-range forecast model, *Mon. Weather Rev.*, *124*(10), 2322–2339, doi:10.1175/1520-0493(1996)124<2322:NBLVDI>2.0.CO;2.

Hrachowitz, M., H. Savenije, T. A. Bogaard, D. Tetzlaff, and C. Soulsby (2013), What can flux tracking teach us about water age distribution patterns and their temporal dynamics?, *Hydrol. Earth Syst. Sci.*, *17*(2), 533–564, doi:10.5194/hess-17-533-2013.

Huntington, T. G. (2006), Evidence for intensification of the global water cycle: Review and synthesis, *J. Hydrol.*, *319*(1–4), 83–95, doi:10.1016/j.jhydrol.2005.07.003.

IPCC (2014), *Climate Change 2013–The Physical Science Basis*, 1535, Cambridge Univ. Press, Cambridge.

James, P. (2003), A 15-year climatology of stratosphere-troposphere exchange with a Lagrangian particle dispersion model 2. Mean climate and seasonal variability, *J. Geophys. Res.*, *108*(D12), 8522, doi:10.1029/2002JD002639.

Jasechko, S., Z. D. Sharp, J. J. Gibson, S. J. Birks, Y. Yi, and P. J. Fawcett (2013), Terrestrial water fluxes dominated by transpiration, *Nature*, *496*(7445), 347–50, doi:10.1038/nature11983.

Jiao, L. (2009), Scientists line up against dam that would alter protected wetlands, *Science*, *326*(5952), 508–509, doi:10.1126/science.326_508.

Jung, M., M. Reichstein, and A. Bondeau (2009), Towards global empirical upscaling of FLUXNET eddy covariance observations: Validation of a model tree ensemble approach using a biosphere model, *Biogeosciences*, *6*(10), 2001–2013, doi:10.5194/bg-6-2001-2009.

Jung, M., et al. (2010), Recent decline in the global land evapotranspiration trend due to limited moisture supply, *Nature*, *467*(7318), 951–954, doi:10.1038/nature09396.

Jung, M., et al. (2011), Global patterns of land-atmosphere fluxes of carbon dioxide, latent heat, and sensible heat derived from eddy covariance, satellite, and meteorological observations, *J. Geophys. Res.*, *116*, G00J07, doi:10.1029/2010JG001566.

Knoche, H. R., and H. Kunstmann (2013), Tracking atmospheric water pathways by direct evaporation tagging: A case study for West Africa, *J. Geophys. Res. Atmos.*, *118*(22), 12,345–12,358, doi:10.1002/2013JD019976.

Kunstmann, H., and G. Jung (2007), Influence of soil-moisture and land use change on precipitation in the Volta Basin of West Africa, *Int. J. River Basin Manag.*, *5*(1), 9–16, doi:10.1080/15715124.2007.9635301.

Läderach, A., and H. Sodemann (2016), A revised picture of the atmospheric moisture residence time, *Geophys. Res. Lett.*, *43*, 924–933, doi:10.1002/2015GL067449.

Lohmann, D., and E. F. Wood (2003), Timescales of land surface evapotranspiration response in the PILPS phase 2(c), *Global Planet. Change*, *38*, 81–91, doi:10.1016/S0921-8181(03)00007-9.

McGuire, K. J., and J. J. McDonnell (2006), A review and evaluation of catchment transit time modeling, *J. Hydrol.*, *330*(3–4), 543–563, doi:10.1016/j.jhydrol.2006.04.020.

Mlawer, E. J., S. J. Taubman, P. D. Brown, M. J. Iacono, and S. A. Clough (1997), Radiative transfer for inhomogeneous atmospheres: RRTM, a validated correlated-k model for the longwave, *J. Geophys. Res.*, *102*(D14), 16,663–16,682, doi:10.1029/97JD00237.

Numaguti, A. (1999), Origin and recycling processes of precipitating water over the Eurasian continent: Experiments using an atmospheric general circulation model, *J. Geophys. Res.*, *104*(D2), 1957–1972, doi:10.1029/1998JD200026.

Reisner, J., R. M. Rasmussen, and R. T. Bruintjes (1998), Explicit forecasting of supercooled liquid water in winter storms using the MM5 mesoscale model, *Q. J. R. Meteorol. Soc.*, *124*(548), 1071–1107, doi:10.1002/qj.49712454804.

Schlesinger, W. H., and S. Jasechko (2014), Transpiration in the global water cycle, *Agric. For. Meteorol.*, *189–190*, 115–117, doi:10.1016/j.agrformet.2014.01.011.

Scott, R., D. Entekhabi, R. Koster, and M. Suarez (1997), Timescales of land surface evapotranspiration response, *J. Climate*, *10*, 559–566, doi:10.1175/1520-0442(1997)010<0559:TOLSER>2.0.CO;2.

Shankman, D., B. D. Keim, and J. Song (2006), Flood frequency in China's Poyang Lake region: Trends and teleconnections, *Int. J. Climatol.*, *26*(9), 1255–1266, doi:10.1002/joc.1307.

Shankman, D., B. D. Keim, T. Nakayama, R. Li, D. Wu, and W. C. Remington (2012), Hydroclimate analysis of severe floods in China's Poyang Lake region, *Earth Interact.*, *16*(14), 1–16, doi:10.1175/2012EI000455.1.

Sodemann, H., H. Wernli, and C. Schwierz (2009), Sources of water vapour contributing to the Elbe flood in August 2002-A tagging study in a mesoscale model, *Q. J. R. Meteorol. Soc.*, *135*(638), 205–223, doi:10.1002/qj.374.

Trenberth, K. E. (1998), Atmospheric moisture residence times and cycling: Implications for rainfall rates and climate change, *Clim. Change*, *39*(4), 667–694, doi:10.1023/A:1005319109110.

Trenberth, K. E. (1999), Conceptual framework for changes of extremes of the hydrological cycle with climate change, *Clim. Change*, *42*(1), 327–339, doi:10.1023/A:1005488920935.

Trenberth, K. E., D. P. Stepaniak, and J. M. Caron (2000), The global monsoon as seen through the divergent atmospheric circulation, *J. Clim.*, *13*(22), 3969–3993, doi:10.1175/1520-0442(2000)013<3969:TGMAST>2.0.CO;2.

Tuinenburg, O. A., R. W. A. Hutjes, and P. Kabat (2012), The fate of evaporated water from the Ganges basin, *J. Geophys. Res.*, *117*(D01107), doi:10.1029/2011JD016221.

van der Ent, R. J., and H. H. G. Savenije (2011), Length and time scales of atmospheric moisture recycling, *Atmos. Chem. Phys.*, *11*(5), 1853–1863, doi:10.5194/acp-11-1853-2011.

van der Ent, R. J., O. A. Tuinenburg, H.-R. Knoche, H. Kunstmann, and H. H. G. Savenije (2013), Should we use a simple or complex model for moisture recycling and atmospheric moisture tracking?, *Hydrol. Earth Syst. Sci.*, *17*(12), 4869–4884, doi:10.5194/hess-17-4869-2013.

van der Ent, R. J., L. Wang-Erlandsson, P. W. Keys, and H. H. G. Savenije (2014), Contrasting roles of interception and transpiration in the hydrological cycle–Part 2: Moisture recycling, *Earth Syst. Dyn.*, *5*(2), 471–489, doi:10.5194/esd-5-471-2014.

Wang-Erlandsson, L., R. J. van der Ent, L. J. Gordon, and H. H. G. Savenije (2014), Contrasting roles of interception and transpiration in the hydrological cycle–Part 1: Temporal characteristics over land, *Earth Syst. Dyn.*, *5*(2), 441–469, doi:10.5194/esd-5-441-2014.

Wei, J., H. R. Knoche, and H. Kunstmann (2015), Contribution of transpiration and evaporation to precipitation: An ET-Tagging study for the Poyang Lake region in Southeast China, *J. Geophys. Res. Atmos.*, *120*(14), 6845–6864, doi:10.1002/2014JD022975.

Wei, Z., K. Yoshimura, A. Okazaki, K. Ono, W. Kim, M. Yokoi, and C. Lai (2016), Understanding the variability of water isotopologues in near-surface atmospheric moisture over a humid subtropical rice paddy in Tsukuba, Japan, *J. Hydrol.*, *533*, 91–102, doi:10.1016/j.jhydrol.2015.11.044.

Wu, S., Y. Yin, D. Zheng, and Q. Yang (2006), Moisture conditions and climate trends in China during the period 1971–2000, *Int. J. Climatol.*, *26*(2), 193–206, doi:10.1002/joc.1245.

Yatagai, A., O. Arakawa, K. Kamiguchi, H. Kawamoto, M. I. Nodzu, and A. Hamada (2009), A 44-year daily gridded precipitation dataset for Asia based on a dense network of rain gauges, *Sci. Online Lett. Atmos.*, *5*, 137–140, doi:10.2151/sola.2009-035.

Yatagai, A., K. Kamiguchi, O. Arakawa, A. Hamada, N. Yasutomi, and A. Kitoh (2012), APHRODITE: Constructing a long-term daily gridded precipitation dataset for Asia based on a dense network of rain gauges, *Bull. Am. Meteorol. Soc.*, *93*(9), 1401–1415, doi:10.1175/BAMS-D-11-00122.1.

Ye, J.-S. (2014), Trend and variability of China's summer precipitation during 1955–2008, *Int. J. Climatol.*, *34*(3), 559–566, doi:10.1002/joc.3705.

Zhang, Q., L. Li, Y.-G. Wang, A. D. Werner, P. Xin, T. Jiang, and D. A. Barry (2012), Has the Three-Gorges Dam made the Poyang Lake wetlands wetter and drier?, *Geophys. Res. Lett.*, *39*(20), doi:10.1029/2012GL053431.

Zhou, L.-T. (2011), Impact of East Asian winter monsoon on rainfall over southeastern China and its dynamical process, *Int. J. Climatol.*, *31*(5), 677–686, doi:10.1002/joc.2101.

Zhu, Y., and L. Chen (2002), The relationship between the asian/australian monsoon and ENSO on a quasi-four-year scale, *Adv. Atmos. Sci.*, *19*(4), 727–739, doi:10.1007/s00376-002-0012-1.

Zuber, A. (1986), On the interpretation of tracer data in variable flow systems, *J. Hydrol.*, *86*(1–2), 45–57, doi:10.1016/0022-1694(86)90005-3.